First operational dodecapole correction in the LHC*

J. Dilly,[1,2,†] V. Ferrentino,[1,3] M. Le Garrec,[1,4] E.H. Maclean,[1] L. Malina,[5] T. Persson,[1] T. Pugnat,[1] L. van Riesen-Haupt,[6] F. Soubelet,[1,7] and R. Tomás[1]

[1] *CERN, Geneva, Switzerland*
[2] *Humboldt University of Berlin, Berlin, Germany*
[3] *University of Naples Federico II, Naples, Italy*
[4] *Goethe University Frankfurt, Frankfurt, Germany*
[5] *Deutsches Elektronen-Synchrotron DESY, Germany*
[6] *EPFL, Lausanne, Switzerland*
[7] *University of Liverpool, Liverpool, United Kingdom*

(Dated: January 12, 2023)

Amplitude detuning measurements in the LHC have shown that a significant amount of detuning is generated via feed-down from high-order field errors in the magnets of the experiment insertion regions. This undesired detuning can be detrimental to luminosity production of the machine and is expected to be enhanced in the upcoming high-luminosity upgrade of the collider, the HL-LHC. In this study, we investigate the high-order errors in detail, performing amplitude detuning measurements during the commissioning of the LHC Run 3 and establish operational corrections via feed-down, using for the first time the dodecapole correctors in the insertion region.

Keywords: LHC, HL-LHC, nonlinear dynamics, dodecapole corrections, feed-down, amplitude detuning, tune shift with action

I. INTRODUCTION AND MOTIVATION

Amplitude detuning, also known as "tune shift with amplitude", describes the action-dependent tune shift in a storage ring and has significant impact on the tune footprint of the particle beams in the Large Hadron Collider (LHC), affecting dynamic aperture (DA) and beam lifetime [1, 2]. It also influences the performance of beam instrumentation [2] and the control of Landau damping. Landau damping of head-tail instabilities is induced by dedicated octupole magnets (Landau Octupoles or MOs) in the arcs around the LHC [3].

To first order in field strength and first order in action, detuning is generated by normal octupole fields, weighted by powers of the β-functions at the octupole sources [4, 5] (see Section II C). Reduction of undesired detuning from octupole errors therefore directly relates to improved control of Landau damping, possibly reducing the necessary powering of the MOs.

It has been established, that in the LHC during proton-proton collisions, the main source of unwanted detuning are normal octupole errors from the quadrupole triplets [2, 6–8] left and right of the experimental insertions of ATLAS at Interaction Point (IP) 1 and CMS at IP5. The beam dynamics in the Insertion Regions (IRs) around the IP are very sensitive to errors, due to their high β-functions, required to reach very small β^*, the value of the β-function at the IP. Error correction in the IRs has therefore been subject to intensive studies during the design phase and in the actual machine, not only in the LHC [2, 7–11], but in most synchroton colliders, such as the Tevatron [12], RHIC [13], SuperKEKB [14] and in the Future Circular Collider [15–17]. One of the upgrades envisioned for the High-Luminosity LHC (HL-LHC) [18], are triplets with larger aperture, increasing the coil aperture from 70 mm in the LHC [6] to 150 mm. This allows for a doubling of the β-function in the triplets, supporting β^* down to 15 cm [19] to raise collision rates and hence the name-giving high luminosity. Yet this change elevates the already high sensitivity to errors in this region [20, 21]. The search and testing for suitable correction targets for increasingly higher field orders has been a long ongoing journey at the LHC [8, 22–25].

The regions of the LHC housing the triplets are occupied by common-aperture magnets, meaning both circulating beams, named Beam 1 and Beam 2, share a single aperture between the so-called separation dipoles, which divide the beams again into their individual beamlines. The nonlinear correction packages [6] are located close to the triplets [2] within this region. A schematic of an IR of the LHC is given in Fig. 1. Any correction needs hence to be valid for both beams.

One of the observables targeted to correct IR-errors has been amplitude detuning. Amplitude detuning is a global parameter and therefore cannot display the individual contribution of each IP to the total detuning. To determine the origin of the errors, local orbit bumps have been introduced during measurements, generating feed-down (see Section II B) to tune and coupling which could then be mitigated using the octupole correctors within the nonlinear correction packages in each IR. Performing this correction has also led to immediate improvements in the performance of beam instrumentation, e.g. in the accuracy of the coupling measurement and the signal-to-noise ratio of the base-band tune (BBQ [26–28]) sys-

* this work has been supported by the HiLumi Project and has been sponsored by the Wolfgang Gentner Programme of the German Federal Ministry of Education and Research

† joschua.dilly@cern.ch

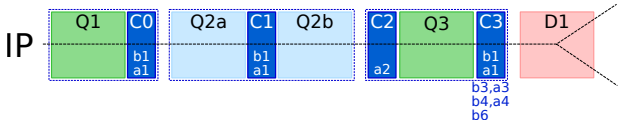

FIG. 1. Schematic of one side of a LHC IR region, showing the common-aperture magents: Q1, Q2a/b and Q3 are the triplet quadrupoles, C0-C3 the corrector packages with the field order to be corrected indicated (see Section II A). D1 is the separation dipole, diverging Beam 1 and Beam 2 to their respective beamlines. Blue lines mark common cryostats. The non-linear corrector package, containing the dodecapole correctors, is included in C3.

tem [2].

During LHC commissioning in 2018, upon changing the crossing scheme from flat-orbit to the operational scheme (see Table I), an increase in amplitude detuning was measured (see Table II and [29, 30]). Further investigation [31] during Machine Development (MD) sessions confirmed this finding and revealed the main contribution to be feed-down from high-order errors, i.e. decapole and dodecapole errors and above, to the octupole fields, due to the crossing schemes in IP1 and IP5. While feed-down to tune from dodecapole fields induced by orbit bumps had been observed in other colliders [32], there have been no measurements of feed-down to first-order amplitude detuning outside of the LHC.

As the influence of the feed-down of magnetic fields depends on the (small) orbit offset raised to the power of the field's order (see Section II B), field errors higher than dodecapole errors are ignored in the here presented study. Also sextupole errors and feed-down to them are omitted in the following discussion: not only are they less affected by feed-down from the high-order errors compared to octupole fields (see again Section II B), they also contribute only in second order in field strengths to amplitude detuning [4] and their correction has been discussed in e.g. [2, 7, 33, 34].

Dodecapole fields on the other hand are the first allowed harmonic of quadrupole magnets [35] and also contribute directly to second-order amplitude detuning (see Section II C). The harmful influence of decapole and dodecapole errors on dynamic aperture and beam lifetime in the upcoming HL-LHC has been shown in simulations and dedicated measurements, in which the normal dodecapole errors were artificially increased to replicate the HL-LHC conditions [25, 36–40].

In this paper detuning measurements are presented, which have been performed in 2022 during LHC commissioning and in a dedicated MD session (with the ID MD6863), confirming the observed errors still to be present in LHC Run 3. Important machine settings for these measurements are shown in Table I and a summary of the measured detuning terms can be found in Table II. A correction option, previously only researched in simulations [37], is explored: Normal dodecapole errors in the IRs are corrected using the observed change in amplitude detuning from feed-down, by in turn utilizing the feed-down to normal octupoles from the dodecapole correctors in the nonlinear corrector packages of the IRs, which had been hitherto inactive during operation.

While measurements and corrections of magnetic fields up to dodecapole order, based on tune shifts using the feed-down artificially introduced by orbit bumps, had also been attempted at RHIC [32], these corrections were never (or only partially) used operationally, as they were detrimental to beam lifetime. On the other hand, a 4 % increase of integrated luminosity was achieved using decapole and dodecapole correctors by targeting beam lifetime directly [41]. So while this is not the first time a particle collider uses dodecapole correctors operationally, it is the first time targeting the feed-down to amplitude detuning and hence also controlling Landau damping. For the LHC this is in fact also the first time these correctors are used in operation.

This paper is structured as follows: In Section II theoretical background, notations and conventions are introduced, as well as the procedure for measurements, simulations and corrections outlined. This is followed by the actual presentation and discussion of the results in Section III. Conclusions are drawn in Section IV, in which also outlook for further studies is suggested.

II. BACKGROUND

A. Field Strengths

The multipole expansion of a general magnetic field $\vec{B} = (B_x, B_y)$ in the planes x (horizontal) and y (vertical), into normal (B_n) and skew (A_n) field components of $2n$-poles, reads

$$B_y + iB_x = \sum_{n=1}^{\infty} (B_n + iA_n)\,(x+iy)^{n-1} \quad . \tag{1}$$

With Eq. (1) this paper follows the convention of using $n = 1$ to indicate a dipole field. Extracting the main field component B_N of a normal 2N-pole magnet, the expansion can be rewritten using b_n and a_n to represent normal and skew relative field errors at the reference radius R_{ref}:

$$B_y + iB_x = \mathrm{B}_N \cdot \sum_{n=1}^{\infty} (b_n + ia_n) \left(\frac{x+iy}{R_{\mathrm{ref}}}\right)^{n-1} \quad , \tag{2}$$

and equivalently for A_N, the main field component of a skew 2N-pole magnet. b_n and a_n are dimensionless but usually given in 'units' of 10^{-4}. As the correction described below makes use of normal dodecapole magnets and is mostly aimed at correcting the b_6 error components (see Section III B), the shorthand "b_6 correction" is employed in the figures and tables of this paper. The normal field component B_n of a normal 2N-pole magnet is then

$$B_n\,[\mathrm{Tm}^{1-n}] = \mathrm{B}_N \cdot \frac{b_n}{R_{\mathrm{ref}}^{n-1}} \tag{3}$$

TABLE I. Machine Settings used during measurements. Crossing is given in half-angles. The horizontal plane is X, the vertical plane is Y. MD3311 is the machine development session in 2018 [31] first investigating the feed-down from high-order errors, MD6863 the session in 2022 dedicated to dodecapole corrections.

Tunes:		$Q_x = 62.28$,	$Q_y = 60.31$		
Optics:		$\beta^* = 30$ cm round optics ($\beta_x^* = \beta_y^*$)			
Commissioning		28 . 04 . 2018			*full crossing*
Energy:		6.5 TeV			
Crossing:	IP-Plane	IP1-Y	IP2-Y	IP5-X	IP8-X
	µrad	160	200	160	–250
Separation:	IP-Plane	IP1-X	IP2-X	IP5-Y	IP8-Y
	mm	–0.55	1.4	0.55	1.0
MD3311		16 . 06 . 2018			*IP5 crossing*
Energy:		6.5 TeV			
Crossing:	IP-Plane	IP5-X			
	µrad	160			
Separation	IP-Plane	– IP5-Y –			
& Offset:	mm	0.55	–1.8		
Commissioning		09 . 05 . 2022			*full crossing*
Energy:		6.8 TeV			
Crossing:	IP-Plane	IP1-Y	IP2-Y	IP5-X	IP8-X
	µrad	–150	0	150	0
Separation:	IP-Plane	IP1-X	IP2-X	IP5-Y	IP8-Y
	mm	0	0	0	0
Commissioning		04 . 06 . 2022			*full crossing*
& MD6863		24 . 06 . 2022			*full crossing*
Energy:		6.8 TeV			
Crossing:	IP-Plane	IP1-Y	IP2-Y	IP5-X	IP8-X
	µrad	-160	200	160	–200
Separation:	IP-Plane	IP1-X	IP2-X	IP5-Y	IP8-Y
	mm	0	1.0	0	1.0
MD6863		24 . 06 . 2022			*IP5 crossing*
Energy:		6.8 TeV			
Crossing:	IP-Plane	IP1-Y	IP2-Y	IP5-X	IP8-X
	µrad	0	200	±160	–200
Separation:	IP-Plane	IP1-X	IP2-X	IP5-Y	IP8-Y
	mm	0	1.0	0	1.0

and similar for skew field components A_n, as well as the skew and normal components of a skew 2N-pole magnet.

It is customary to normalize the field strengths of Eq. (3) to the magnetic rigidity $B\rho$, defined by the main dipole field B of the accelerator and its bending radius ρ:

$$K_n\,[\mathrm{m}^{-n}] = \frac{B_n}{B\rho}\,(n-1)! \qquad \text{and}$$
$$J_n\,[\mathrm{m}^{-n}] = \frac{A_n}{B\rho}\,(n-1)!\,. \tag{4}$$

B. Feed-Down

The effect of feed-down occurs when a particle beam's orbit passes off-center through a magnet, due to either a transverse misalignment of the magnet or an off-center closed orbit of the beam itself. In these cases, the magnetic field can be described as a composition of the current order main field plus lower order components, and can be understood by applying a Taylor expansion on x and y in Eq. (1) or, equivalently, the Hamiltonian of the system in curvilinear (comoving) coordinates. These additional components therefore cause the same effects on the beam as lower order sources would [43]. Using Eq. (1) and Eq. (4), and with $(\Delta x,\, \Delta y)$ being the orbit of the off-center particle, feed-down to field order $n \geq 1$ from fields up to order $n + P$ can be expressed as:

$$(K_n + iJ_n)^{\text{w/ feed-down}} = \sum_{p=0}^{P}(K_{n+p} + iJ_{n+p})\frac{(\Delta x + i\Delta y)^p}{p!}. \tag{5}$$

C. Amplitude Detuning from Dodecapoles

Using the invariant of motion $\epsilon_u = 2J_u$, with the action J_u, the amplitude $\mathcal{A}_u(s)$ of a particle in the transversal plane $u \in \{x, y\}$ at longitudinal position s is

$$\mathcal{A}_u(s) = \sqrt{2J_u\beta_u(s)} = \sqrt{\epsilon_u\beta_u(s)}\,. \tag{6}$$

The dependency of the tune on amplitude is usually given with respect to this invariant and is therefore location independent. The detuning coefficients can be expressed via Taylor expansion of the tune Q_u around the unperturbed tune at zero-action Q_{u0}; explicitly stated up to second order in amplitude:

$$Q_u(\epsilon_x, \epsilon_y) = Q_{u0} + \frac{\partial Q_u}{\partial \epsilon_x}\epsilon_x + \frac{\partial Q_u}{\partial \epsilon_y}\epsilon_y + \frac{1}{2!}\left(\frac{\partial^2 Q_u}{\partial \epsilon_x^2}\epsilon_x^2 + 2\frac{\partial^2 Q_u}{\partial \epsilon_x \partial \epsilon_y}\epsilon_x\epsilon_y + \frac{\partial^2 Q_u}{\partial \epsilon_y^2}\epsilon_y^2\right) + \ldots \tag{7}$$

To numerically compute detuning integrals, a thin lens approximation is used in which multipole elements are split into single kicks at s_w surrounded by drift spaces; the kick strength being $K_n L_w$ - the integrated strength $K_n(s)$ (see Eq. (4)) over the length L_w of element w. β-function and orbit are then also approximated using the value at s_w. In this approximation, the contribution to the first-order terms of Eq. (7) from octupole fields of element w with integrated strength $K_4 L_w$ can be calcu-

TABLE II. Summary of amplitude detuning measurements from 2018 [29–31] at 6.5 TeV and $\beta^*=0.3$ m and 2022 at 6.8 TeV and $\beta^*=0.3$ m. Detailed orbit setups are described in Table I while here the measurements are identified by either "flat-orbit" (i.e. crossing bumps deactivated) or which of IP1 and IP5 are activated and at ("@") which half-angle. If both IPs are mentioned with different signs, the top sign refers to IP1 and the bottom sign to IP5. The four detuning terms are abbreviated as in Eq. (11): $Q_{a,b} = \partial Q_a/\partial(2J_b)$. Measurements for Beam 1 are shown in blue (top) and for Beam 2 in red (bottom). Where AC-Dipole kicks were used, the results have been corrected for the effect of forced oscillations [42].

	$Q_{x,x}$ [10^3 m^{-1}]	$Q_{y,x}$ [10^3 m^{-1}]	$Q_{x,y}$ [10^3 m^{-1}]	$Q_{y,y}$ [10^3 m^{-1}]
2018 MD3311	0.8 ± 0.5	10 ± 1	6 ± 2	20 ± 5
flat-orbit	-7.5 ± 0.5	8 ± 2	-2 ± 1	6 ± 1
2018 Commissioning	34 ± 1	8 ± 2	18 ± 1	-38 ± 1
IP1&5 xing @ +160 µrad	-3 ± 1	-10 ± 3	-14 ± 2	13 ± 3
2018 MD3311	56 ± 6	-9 ± 15	-78 ± 7	2.5 ± 0.8
IP5 xing @ +160 µrad	1.5 ± 0.5	4 ± 1	-4 ± 3	12 ± 1
2022 Commissioning w/o b_6	-15.4 ± 0.9	32.2 ± 0.2	33.7 ± 1.0	-8.4 ± 0.5
flat-orbit	-8.7 ± 0.7	13 ± 2	-3 ± 2	10.0 ± 0.9
2022 Commissioning w/o b_6	20 ± 4	43 ± 4	33 ± 10	-10 ± 3
IP1&5 xing @ ∓150 µrad	26.0 ± 0.8	-31 ± 3	-27 ± 4	18 ± 7
2022 Commissioning w/ b_6	-34 ± 7	38 ± 3	24 ± 4	-6 ± 1
flat-orbit	-15 ± 2	10 ± 3	6.3 ± 0.4	-3.6 ± 0.6
2022 Commissioning w/ b_6	-21 ± 4	47 ± 2	56 ± 6	15 ± 1
IP1&5 xing @ ∓160 µrad	-28 ± 2	22 ± 4	13 ± 2	-7.8 ± 0.5
2022 MD6863 w/o b_6	-18 ± 2	32 ± 2	22 ± 4	0.0 ± 0.9
flat-orbit	-19.2 ± 1.7	13.1 ± 1.7	12 ± 2	3.4 ± 0.8
2022 MD6863 w/o b_6	9 ± 2	36.8 ± 2.0	27 ± 2	2.1 ± 1.0
IP1&5 xing @ ∓160 µrad	20.9 ± 1.1	-39 ± 2	-42.7 ± 1.6	19.7 ± 1.3
2022 MD6863 w/o b_6	23 ± 2	1 ± 2	-3.7 ± 1.2	3.0 ± 1.4
IP5 xing @ +160 µrad	10.6 ± 1.2	-8 ± 3	-15.8 ± 1.6	5.3 ± 1.2
2022 MD6863 w/o b_6	8.9 ± 1.4	4 ± 3	-0.9 ± 0.5	0.3 ± 0.5
IP5 xing @ −160 µrad	20.3 ± 1.7	-15 ± 4	-23.3 ± 1.7	-1.5 ± 1.6
2022 MD6863 w/ b_6	-12.7 ± 1.0	33 ± 2	30.1 ± 1.0	17.5 ± 1.4
IP1&5 xing @ ∓160 µrad	-46 ± 4	31 ± 2	34.5 ± 1.4	-17.9 ± 1.0

lated [44] as

$$\frac{\partial Q_x}{\partial(2J_x)} = \sum_w \frac{K_4 L_w}{32\pi}\,\beta_x^2(s_w) \tag{8a}$$

$$\frac{\partial Q_x}{\partial(2J_y)} = \frac{\partial Q_y}{\partial(2J_x)} = \sum_w -\frac{K_4 L_w}{16\pi}\,\beta_x(s_w)\beta_y(s_w) \tag{8b}$$

$$\frac{\partial Q_y}{\partial(2J_y)} = \sum_w \frac{K_4 L_w}{32\pi}\,\beta_y^2(s_w)\,. \tag{8c}$$

Including feed-down, as in Eq. (5), from normal and skew decapoles (K_5L, J_5L) and normal and skew dodecapoles (K_6L, J_6L) we get due to the orbit $\Delta x(s_w), \Delta y(s_w)$ at an element w

$$\begin{aligned}(K_4 L_w)^{\text{w/ feed-down}} = \\ K_4 L_w + \Delta x(s_w) K_5 L_w - \Delta y(s_w) J_5 L_w + \\ \frac{1}{2}\left(\Delta x(s_w)^2 - \Delta y(s_w)^2\right) K_6 L_w - \Delta x(s_w)\Delta y(s_w) J_6 L_w\,.\end{aligned} \tag{9}$$

Normal dodecapole magnetic fields also contribute directly and linearly to the second-order detuning terms of Eq. (7) in the following manner:

$$\frac{\partial^2 Q_x}{\partial(2J_x)^2} = \sum_w \frac{K_6 L_w}{384\pi}\,\beta_x^3(s_w) \tag{10a}$$

$$\frac{\partial^2 Q_x}{\partial(2J_x)\partial(2J_y)} = \frac{\partial^2 Q_y}{\partial(2J_x)^2} = \sum_w -\frac{K_6 L}{128\pi}\,\beta_x^2(s_w)\beta_y(s_w) \tag{10b}$$

$$\frac{\partial^2 Q_x}{\partial(2J_y)^2} = \frac{\partial^2 Q_y}{\partial(2J_x)\partial(2J_y)} = \sum_w \frac{K_6 L_w}{128\pi}\,\beta_x(s_w)\beta_y^2(s_w) \tag{10c}$$

$$\frac{\partial^2 Q_y}{\partial(2J_y)^2} = \sum_w -\frac{K_6 L_w}{384\pi}\,\beta_y^3(s_w)\,. \tag{10d}$$

For brevity, in the following we will use the symbols

$$Q_{a,b} = \frac{\partial Q_a}{\partial(2J_b)} \quad \text{and} \quad Q_{a,bc} = \frac{\partial^2 Q_a}{\partial(2J_b)\partial(2J_c)}, \tag{11}$$

as well as short-hands for the coefficients

$$\tilde{\beta}_{a,b} = \begin{cases} \tilde{\beta}_{x,x} = \frac{\beta_x^2}{32\pi} \\ \tilde{\beta}_{x,y} = -\frac{\beta_x \beta_y}{16\pi} \\ \tilde{\beta}_{y,y} = \frac{\beta_y^2}{32\pi} \end{cases} \text{ and } \tilde{\beta}_{a,bc} = \begin{cases} \tilde{\beta}_{x,xx} = \frac{\beta_x^3}{384\pi} \\ \tilde{\beta}_{x,xy} = -\frac{\beta_x^2 \beta_y}{128\pi} \\ \tilde{\beta}_{x,yy} = \frac{\beta_x \beta_y^2}{128\pi} \\ \tilde{\beta}_{y,yy} = -\frac{\beta_y^3}{384\pi} \end{cases}, \tag{12}$$

with $a, b, c \in \{x, y\}$.

D. Measurements

While in the beginning of LHC operation, amplitude detuning has been measured based on free oscillations following a single dipole "kick" [45], in later years they were achieved using forced oscillations with an AC-Dipole [42, 46, 47]. Optics measurements with AC dipoles had already been tested at RHIC [48, 49], and in the SPS in preparation for LHC optics measurements [50–52].

The oscillations, close to the tune frequency, are adiabatically ramped up and down to and from the desired amplitude [42, 53, 54]. Exciting single pilot bunches ($\approx 10^{10}$ protons) per beam, this method allows for measurements at top-energy without endangering machine safety and without beam decoherence or emittance growth. This means, a single bunch can be excited multiple times without having to go through the time-consuming process of dumping the blown-up beam, ramping down the magnets to injection settings, refilling the proton bunches, ramping to top-energy again and performing the optics-squeeze (i.e. the reduction of β^* to the desired value). The transverse positions of the beam centroid over approximately 6600 turns are captured during the AC-Dipole's flat-top at each Beam Position Monitor (BPM) [55] and then analysed. Due to the use of the AC-Dipole the first-order amplitude detuning direct terms $Q_{x,x}$ (Eq. (8a)) and $Q_{y,y}$ (Eq. (8c)) will be enhanced by a factor of 2, while the second-order direct terms $Q_{x,xx}$ (Eq. (10a)) and $Q_{y,yy}$ (Eq. (10d)) are enhanced by a factor of 3 [42]. All detuning data presented in this paper are compensated for these factors and detuning terms quoted are the "free" detuning of the machine. In principle, also the second-order terms $Q_{x,xy}$ and $Q_{y,xy}$ are doubled during forced oscillations, yet only the tune shift with the action of one plane has been measured during the here presented study and these terms have therefore not been investigated.

AC-Dipole excitations are generally performed in the two transverse planes at the same time to be able to measure both tunes. The amplitude of one plane is kept low and constant, while slowly increasing the strength, i.e. action, of the other plane. The $\Delta_Q = |Q_{\text{natural}} - Q_{\text{driven}}|$ of the plane with constant amplitude kicks is usually smaller than the other, to increase signal-strength of the tune line even at these low amplitudes due to the decreased adiabaticity of the ramp. In the other plane, the driven tune is kept slightly further apart to avoid exciting diagonal ($\Delta_{Q_x} = \Delta_{Q_y}$) resonances [56, 57]. The amplitude is increased within the amplitude range of the AC-Dipole only in small steps and only until first losses at the collimators can be seen, to not risk a beam dump and to not lose beam intensity, needed to ensure good signals in the subsequent measurements. When the available kick amplitude has been exploited, the procedure is repeated with the roles of the planes switched.

E. Data Analysis

The resulting turn-by-turn data is then processed by our python software tools [58]: Cleaning is done automatically via a specialized Singular-Value-Decomposition (SVD) and Fourier transform on the signal [59, 60], followed by a combination of automated and manual cleaning steps to remove faulty BPMs and ascertain the correct tune-line in the spectrum [61]. In preparation for extensive amplitude detuning studies like the one presented, these latter methods have recently been extended with new features, such as automated BPM cleaning (via the *Outlier Filter* described below) and an option for manual spectral-line selection. This has allowed for fast online (i.e. during measurements) analysis of the data during the MD, which had not been possible to this level in the past.

Outlier Filter The outlier filtering function [59] is utilized at multiple stages of the data analysis and operates in the following way: The function gets an array x of data of length n_x, which can be any scalar data but in the context of this paper has been data of the tunes, either measured per BPM or a time series from the BBQ. It removes data points in the tails of the measured distribution, which are too populated assuming x_n to be samples from a normal distribution, specified by measured mean and standard deviation of the given data, due to the finite sample size n_x. A data point, outside of a user-specified limit, is removed if there is less than a 50 % chance that it stems from the specified normal distribution. This filtering method is first applied to filter out BPMs for which the driven or natural tunes were not correctly identified and later to clean the tune data from the BBQ, used to establish the baseline for the machine tune at zero-action (see Section II E).

Action The action $2J$ is calculated at each BPM at location s from the amplitude $\mathcal{A}_{\text{BPM}}$ of the main line of the BPM-spectrum (i.e. the driven tune) via

$$2J_{\text{BPM}} = \frac{\mathcal{A}_{\text{BPM}}^2}{\beta_{\text{model}}(s)} \, . \tag{13}$$

Instead of the β-function from the model (as in [62]), the measured β values can also be used as shown in [63], yet this feature has not yet been implemented in the analysis code. Due to the low β-beating in the machine [64, 65] using the model β-function is still justified.

The action is further rescaled to perform beam-based adjustments for residual BPM calibration errors [63], by the mean ratio of the β-function estimated from phases [66] and the β-function from amplitudes [62] at the arc BPMs per kick.

The error on the action $\delta 2J_{\mathrm{BPM}}$ can be acquired from the error on the amplitude $\delta\mathcal{A}_{\mathrm{BPM}}$, which in turn is estimated from the noise on the signal:

$$\delta\mathcal{A}_{\mathrm{BPM}} = \sqrt{\frac{2}{N_{\mathrm{Turns}}}} \cdot \mathrm{R}_{\mathrm{BPM}}^{(\mathrm{cleaned})} \ . \tag{14}$$

N_{Turns} is the number of turns over which the measurement is recorded and $\mathrm{R}_{\mathrm{BPM}}^{(\mathrm{cleaned})}$ is the estimated BPM-Resolution of the cleaned signal. Here, BPM-Resolution is defined as the standard deviation of the noise, which is first estimated by the difference between the cleaned signal and the original signal at the BPM (as $\mathrm{R}_{\mathrm{BPM}}^{(\mathrm{raw})}$). On this estimate a coefficient has been matched via an empirical study, targeting e.g. the ratio of the noise floor levels in the frequency spectra of raw data and SVD-cleaned data:

$$\mathrm{R}_{\mathrm{BPM}}^{(\mathrm{cleaned})} = \frac{1}{\sqrt{2}\cdot 10} \cdot \mathrm{R}_{\mathrm{BPM}}^{(\mathrm{raw})} \ . \tag{15}$$

With Eqs. (13) and (14) we can calculate the error on the action:

$$\delta 2J_{\mathrm{BPM}} = \frac{2\cdot\mathcal{A}_{\mathrm{BPM}}\cdot\delta\mathcal{A}_{\mathrm{BPM}}}{\beta_{\mathrm{model}}(s)} \ . \tag{16}$$

From these estimates at each BPM for actions $2J_{\mathrm{BPMs}} = \{2J_{\mathrm{BPM_1}}, ..., 2J_{\mathrm{BPM_N}}\}$ and corresponding errors $\delta 2J_{\mathrm{BPMs}} = \{\delta 2J_{\mathrm{BPM_1}}, ..., \delta 2J_{\mathrm{BPM_N}}\}$, we want to get an estimate for the actual action and the error we might be making on this estimation.

We can use inverse-variance weighting to define an error-weighted average of a set of measurements $x = \{x_1, ..., x_N\}$ and their associated errors $\delta x = \{\delta x_1, ..., \delta x_N\}$

$$\langle x\rangle_\delta = \frac{1}{\sum_{n=1}^{N}\frac{1}{\delta x_n^2}}\sum_{n=1}^{N}\frac{x_n}{\delta x_n^2} = \frac{1}{S_\delta(x)}\sum_{n=1}^{N}\frac{x_n}{\delta x_n^2} \ , \tag{17}$$

defining also a sum-of-weights $S_\delta(x)$. Equation (17) is used to get an estimate of the action in the machine:

$$2J = \langle 2J_{\mathrm{BPMs}}\rangle_\delta \ . \tag{18}$$

For the estimation of the error on this quantity, we can calculate the error-weighted variance on the data

$$\sigma_\delta^2(x) = \left\langle |x - \langle x\rangle_\delta|^2 \right\rangle_\delta \tag{19}$$

as well as the variance on $\langle x\rangle_\delta$ itself:

$$\sigma^2(\langle x\rangle_\delta) = \frac{1}{\sum_{n=1}^{N}\frac{1}{\delta x_n^2}} = \frac{1}{S_\delta(x)} \ , \tag{20}$$

and the effective sample size

$$N_\delta(x) = \frac{\left(\sum_{n=1}^{N} 1/\delta x_n^2\right)^2}{\sum_{n=1}^{N}\left(1/\delta x_n^2\right)^2} \ . \tag{21}$$

Also using the abbreviations $\sigma_\delta^2 = \sigma_\delta^2(2J_{\mathrm{BPMs}})$, $N_\delta = N_\delta(2J_{\mathrm{BPMs}})$ and $S_\delta = S_\delta(2J_{\mathrm{BPMs}})$ the error on the action can then be estimated via the unbiased sum of the two above described variances:

$$\delta 2J_{\mathrm{estimated}} = \sqrt{\frac{N_\delta}{N_\delta - 1}\left(\sigma_\delta^2 + \frac{1}{S_\delta}\right)} \ . \tag{22}$$

To account for the measurement's finite sample size, whilst still estimating the standard deviation of a normally distributed quantity (Student's t-distributed with an infinite number of degrees of freedom), the error value is corrected by a multiplicative coefficient. We calculate the coefficient $t_{\mathrm{correction}}$ utilising the cumulative distribution function $F(s, N)$ of Student's t-distribution (with mean equal to 0 and spread equal to 1) as a function of the actual value s and the number of degrees of freedom N.

$$t_{\mathrm{correction}} = F^{-1}(F(1,\infty), N_\delta), \tag{23}$$

which is a factor towards the limiting case $N \to \infty$ for a given confidence level corresponding to 1 σ in the normal distribution.

$$\delta 2J = \delta 2J_{\mathrm{estimated}} \cdot t_{\mathrm{correction}} \ . \tag{24}$$

These statistical functions are part of the `omc3`-package [58]. The calculations are done individually for each transversal plane.

Tune For each BPM the natural tune is identified within a given frequency window as the line with the largest amplitude in that window [60]. Again, the two transversal planes are handled identically and separately. The selected lines are manually confirmed in a spectral plot and can be modified if needed.

The measured natural tune Q_{natural} and its error $\delta Q_{\mathrm{natural}}$ at the time of the excitation is calculated from the selected spectral lines by the mean and standard deviation over the BPMs. The natural tune at zero-action (Q_{u0} in Eq. (7)) is found around each excitation time from the BBQ data logged in the LHC, which removes the influence of possible tune drifts during the measurement duration. The BBQ data is first cleaned using a sliding window of 100 data points, which translates to roughly 15 seconds of data, and applying the *Outlier Filter* described above within each window. This removes measurement outliers of the BBQ as well as the excited tunes

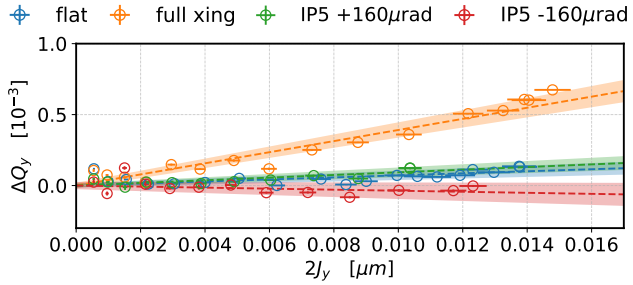

FIG. 2. Data of the measured direct vertical detuning term in Beam 2 without dodecapole correction from MD6863 (Table I). Shown are the scenarios of flat-orbit (blue), with full crossing scheme applied (orange), and with crossing only in IP5 at +160 µrad (green) and −160 µrad (red). Dashed lines show the linear fit to the data points, while the colored area covers one standard deviation of the fit. The constant part of the fit has been subtracted from the fit and its respective data points. These are examples of the measurements of four data points in Table II.

during the AC-Dipole operation, which lasts about 1 s. If a value is removed in any window, it will be completely excluded from analysis. From this filtered data the mean is calculated for each window, resulting in a moving average. This average is in turn subtracted from the data points to calculate a moving standard deviation using the same window lengths. The tunes Q_{BBQ} are then the value of the moving average closest to the kick-times, while the error on those measurements δQ_{BBQ} are the values of the moving standard deviation at the same times. The tune values for the detuning-fit are then

$$\Delta Q_{\text{BBQ-corrected}} = Q_{\text{natural}} - Q_{\mathrm{BBQ}} \tag{25}$$

$$\delta\Delta Q_{\text{BBQ-corrected}} = \sqrt{\delta Q^2 + \delta Q_{\mathrm{BBQ}}^2}\,. \tag{26}$$

Fitting To get the first-order detuning coefficients, the slope of the detuning $\Delta Q_{\text{BBQ-corrected}}$ over the actions $2J$ at different kick-amplitudes and their errors $\delta\Delta Q_{\text{BBQ-corrected}}$ and $\delta 2J$ is fitted to a linear polynomial by means of an orthogonal distance regression (ODR) algorithm [67] provided by the `scipy` python package [68]. ODR also produces an estimated error (one standard deviation) on the fit. In principle also a fit to second-order polynomials is possible, yet, as will be discussed in Section III C, due to the low kick amplitudes in most of the measurements, no usable fits could be obtained.

Examples of the results of the measurement at different crossing angles are given in Fig. 2: depicted are the vertical-plane tune shifts over the vertical-plane actions including their linear ODR fits for four different scenarios, all without dodecapole correction, as performed during the MD in 2022. The resulting fit values and their standard deviation for all relevant measurement scenarios can be found in Table II: the measurement results from 2018 which triggered the study, and from commissioning and the MD in 2022. A discussion of the data is presented in Section III.

F. Correction Approach

The normal dodecapole corrector elements (`MCTX`) left and right of IP1 and IP5 are used to compensate for the measured detuning shift with crossing angle $\Delta Q_{a,b}$. As the contributions to detuning add up linearly, an equation system can be built with these correctors as unknowns, targeting $-\Delta Q_{a,b}$:

$$-\begin{pmatrix} \Delta Q_{a,b}^{(\mathrm{B1})} \\ \Delta Q_{a,b}^{(\mathrm{B2})} \\ \vdots \end{pmatrix} = \begin{pmatrix} M_{a,b;L1}^{(\mathrm{B1})} & M_{a,b;R1}^{(\mathrm{B1})} & M_{a,b;L5}^{(\mathrm{B1})} & M_{a,b;R5}^{(\mathrm{B1})} \\ M_{a,b;L1}^{(\mathrm{B2})} & M_{a,b;R1}^{(\mathrm{B2})} & M_{a,b;L5}^{(\mathrm{B2})} & M_{a,b;R5}^{(\mathrm{B2})} \\ & \vdots & & \end{pmatrix} \cdot \begin{pmatrix} K_6 L_{L1} \\ K_6 L_{R1} \\ K_6 L_{L5} \\ K_6 L_{R5} \end{pmatrix}, \tag{27}$$

where the matrix elements are the detuning coefficients from Eq. (12) with feed-down from K_6 to K_4 (see Eq. (9))

$$M_{a,b;w}^{(\mathrm{B}N)} = \frac{1}{2}\left(\Delta x_w^{(\mathrm{B}N)^2} - \Delta y_w^{(\mathrm{B}N)^2}\right)\tilde{\beta}_{a,b;w}^{(\mathrm{B}N)}\,, \tag{28}$$

using the subscript short-hands LIP, RIP for the corrector elements left and right of IP $\in \{1, 5\}$. B$N \in \{\mathrm{B1}, \mathrm{B2}\}$ indicates the beam. Equation (27) can be extended, as hinted at by the vertical dots, to include multiple targeted detuning terms $\Delta Q_{a,b}$, as well as different setups, e.g. the same detuning term but with different crossing angles. The resulting equation system can then be solved, or the error on the solution minimized, by standard linear optimizers.

Before the data of 2022 could be measured, more complex scenarios, e.g. targeting single IRs or using inequalities, were studied using the 2018 data, which had been presented in [69]. In 2022 all calculations were based on equalities to the measured tune shifts. During commissioning and the MD these were exclusively based on the difference between flat-orbit and with crossing in both IR1 and IR5 (see Table I), due to the data from single IRs not yet being available at the time of the "online" correction calculations. These corrections could be tested and verified in the machine. After the data from the measurements with individual crossing schemes in IR5 (again Table I) had been analyzed, corrections were also calculated taking these into account and are discussed in Section III B.

G. Correction Calculation

In simulations the nominal LHC is recreated in cpymad [70], a python wrapper for `MAD-X` [71], using the Run 3 sequence and $\beta^* = 30$ cm round optics. There are no errors included into the model. The orbit is set up according to the desired realization, as described in Table I.

From the optics functions, acquired using the `TWISS` command in `MAD-X`, and the measurement data the desired equation systems of Eq. (27) are built and a sum-of-squares minimization performed, using the (Moore-Penrose) pseudo-inverse of the matrix build from the $M_{a,b;w}$ derived from the model. The uncertainties on the measurement-fits $\Delta Q_{a,b}$ are propagated to the resulting corrections. To check the validity of the calculations, the obtained corrector strengths are applied to the simulated lattice and the actual detuning change is determined from the `PTC`-module [72, 73] as well as from Eqs. (8) and (9).

The corrections can then be trimmed into the accelerator via the LHC Software Architecture (LSA [74]) and their actual effectiveness evaluated.

III. RESULTS

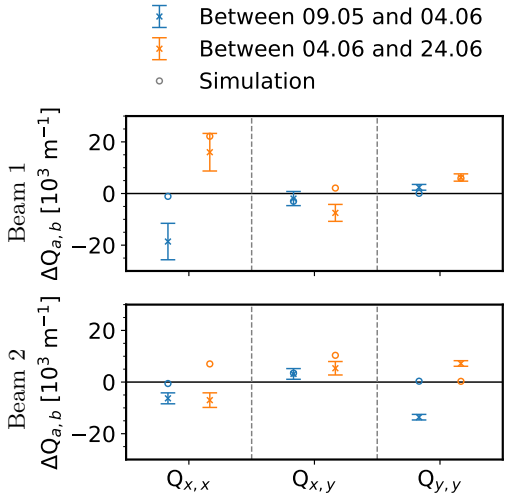

FIG. 3. Differences of detuning at flat orbit in measurement (crosses and errorbars) between the first two measurements (orange) and between the second and third measurement (blue) in 2022 compared to the simulated expected changes from differences in LHC machine settings (circles), using the calculated corrections of "MD6863 w/ IP5" in Table III (with opposite signs) as error sources. The differences between the 09.05 and 04.06 were: crossing schemes in IP2 and IP8, skew and normal sextupole corrections in IP1 and IP5, as well as the "Commissioning 2022" correction, which was active at the time of the second measurement. Between 04.06 and 24.06 the dodecapole correction was deactivated again, but local corrections in the first single-aperture quadrupole (Q4) of Beam 2, corrections of arc 81 and arc 45 in Beam 1, and global β-beating and dispersion corrections for each beam, were applied. Additionally, a waist-shift correction had been applied in Beam 2 at IP5 [75].

During the 2022 LHC commissioning and again for verification and improvement during MD, measurements were performed following the procedure described in Section II D at the top-energy of LHC Run 3 of 6.8 TeV after squeezing the beam to $\beta^* = 30$ cm. All outcomes of these measurements are listed in Table II.

Despite similar machine settings some differences could be seen in the detuning measurements from different dates in 2022. Between measurements various corrections had been applied to the LHC, which are named in Fig. 3. Yet, the expected detuning shifts from these do not seem to replicate the observed differences, as demonstrated for the flat-orbit measurements in Fig. 3.

In contrast to the findings in 2018, large cross-term detuning is present in Beam 1 even at flat-orbit (see Table II), the sources of which have not yet been identified. This is surprising, as between LHC Run 1 and Run 2 the octupole errors had not changed, and in both here presented cases, 2018 and 2022, corrections up to octupole order had been implemented beforehand. These findings have been presented to the LHC Machine Committee (LMC) [76].

A. Dodecapole Corrections

Detuning measurements were carried out first at flat-orbit and then with the full crossing scheme applied, to establish the shift in detuning between the two scenarios. Following Sections II F and II G normal dodecapole corrections were calculated from the resulting detuning shifts, which were then in turn verified by repeating the measurements with powered dodecapole correctors. During commissioning, the measurements were done on two separate occasions, allowing for "offline" analysis of the results, while during the MD the analysis and calculation of corrections were done "online", that is during the measurement period. As the two first-order cross-terms (Eq. (8b)) are referring to the same physical quantity only one value was used in the corrections to give all three detuning terms (Eq. (8)) equal weight. For the corrections during commissioning these values were picked from one of the measurements, based on the quality of the measured data: At flat-orbit the measured value (Table II) of $Q_{x,y}$ was used for Beam 1 and the value of $Q_{y,x}$ for Beam 2. With crossing enabled $Q_{y,x}$ for Beam 1 and $Q_{x,y}$ Beam 2 were used. During the MD a different approach was elected and the average of the measured values $Q_{x,y}$ and $Q_{y,x}$ was designated as correction target. In Figs. 4, 5, 7, 9 and 10 the latter approach is used when the cross-term is presented.

The calculated corrective powering of the dodecapole magnets is presented in Table III, including estimated errors on the correction from the errors on the fits of the measurement and also including the percentage of the maximum absolute powering of the magnets. We can see, that the corrections calculated in commissioning have almost equal powering between left and right in IR5 at 14 % of the maximum strength. There is a stronger powering in IR5 compared to IR1, where a maximum of only 7 % is reached in the right corrector. The corrections from the MD ("MD6863 w/o IP5") are in general slightly increased in comparison: on average 1.5 % in

TABLE III. Dodecapole-corrector strength values (K_6). In parenthesis the percentage of the maximum powering at 6.8 TeV is given. The "w/ IP5" and "w/o IP5" labels on the MD6863 corrections refer to whether the additional measurements of crossing-bumps only around IP5 were taken into account or not (see Section III B). Below also the β-functions at the correctors are given, rounded to meters. The β-symmetries are accurate to below 10 cm.

	IP1		IP5	
	`MCTX.3L1` $[10^3\,\mathrm{m}^{-6}]$	`MCTX.3R1` $[10^3\,\mathrm{m}^{-6}]$	`MCTX.3L5` $[10^3\,\mathrm{m}^{-6}]$	`MCTX.3R5` $[10^3\,\mathrm{m}^{-6}]$
Commissioning 2022	-0.606 ± 0.715 (2%)	-2.696 ± 1.179 (7%)	5.004 ± 0.752 (14%)	-5.053 ± 0.907 (14%)
MD6863 w/o IP5	1.269 ± 0.731 (3%)	-3.288 ± 0.577 (9%)	6.367 ± 0.563 (18%)	-4.087 ± 0.782 (11%)
MD6863 w/ IP5	0.493 ± 0.192 (1%)	-3.982 ± 0.188 (11%)	5.003 ± 0.132 (14%)	-5.032 ± 0.162 (14%)
$\beta_x^{(B1)}$ and $\beta_y^{(B2)}$	3494 m	7177 m	3494 m	7177 m
$\beta_y^{(B1)}$ and $\beta_x^{(B2)}$	7177 m	3494 m	7177 m	3494 m

IR1 and 0.5 % in IR5, reflecting increased detuning shifts (see below). Also, the left-right symmetry in IR5 is broken in these corrections, favouring the left corrector (at 18 %) over the right corrector (at 11 %). Including the IR5 measurements in the correction ("MD6863 w/ IP5", see Section III B), the IR5 symmetry is restored, yet the strength of the corrector right or IP1 is further increased, while the strength of the left corrector almost vanishes.

As none of the powering values are above 18 % of the maximum powering of the magnets, we expect negligible impact on beam lifetime from the powering: they had to be powered to more than a quarter of their maximum strengths to show any measurable effect on lifetime (see [40]), which is discussed and confirmed in Section III E.

Figures 4 and 5 show the measured detuning change introduced by the crossing scheme during commissioning and MD respectively. In blue the detuning change without correction is presented and in both measurements the detuning from high-order errors can be observed. In contrast to what has been measured in 2018, were mostly Beam 1 had been affected, we now see in Beam 1 big changes only in the direct horizontal term ($Q_{x,x}$). In Beam 2 on the other hand, $Q_{x,x}$ and the cross-term $Q_{x,y}$ are majorly spoiled. The strongest feed-down was experienced in the cross-term of Beam 2 during MD, resulting in a change of detuning of more than $50 \cdot 10^3\,\mathrm{m}^{-1}$ in absolute value.

Blue vertical bars show the expected detuning shift to be compensated by the correction, based on the simulation results, and we see that for both corrections the measured data could not be matched perfectly. The expected residual detuning shifts after correction are presented in orange. The figures show that $Q_{x,y}$ and $Q_{y,y}$ in Beam 1 are expected to be slightly spoiled to achieve the partial correction of $Q_{x,x}$ in Beam 1 and very good correction of all terms in Beam 2. In the last column of the figures, the error-weighted root-mean-square (RMS, where the mean is calculated in accordance with Eq. (17)) of all terms is shown, in which the net positive effect of the correction can be recognized easily: Before correction Beam 2 shows a RMS measured tune shift of $34 \cdot 10^3\,\mathrm{m}^{-1}$ (commissioning) and $40 \cdot 10^3\,\mathrm{m}^{-1}$ (MD6863) while the RMS of Beam 1 is much smaller at $19 \cdot 10^3\,\mathrm{m}^{-1}$ (commissioning) and $11 \cdot 10^3\,\mathrm{m}^{-1}$ (MD6863). In turn, Beam 2 is expected to be very well corrected, while Beam 1 will see a lesser improvement, if any.

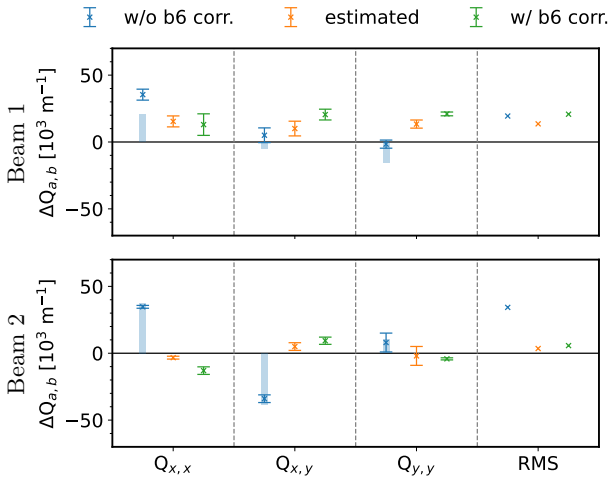

FIG. 4. Detuning shifts as measured during commissioning 2022 between detuning with full crossing and at flat-orbit for all detuning terms and the error-weighted root-mean-square (RMS) over all terms. Measured values for the cross-terms $Q_{x,y}$ and $Q_{y,x}$ have been averaged. Shown in blue is the measurement without dodecaple correction applied as circle with error bars, and the detuning to be compensated by the correction as simulated via the bar. In orange the estimated value after correction is shown. The data in green is the actual measured detuning shift with crossing angle after dodecapole correction.

In green the actual measured detuning shifts still present in the machine after correction are shown. In general, we see that for both corrections all terms have been "over-corrected". This makes the RMS for most measurements worse than expected, yet still resulting in an overall significant improvement: Beam 1 has been slightly spoiled by $+1.3 \cdot 10^3\,\mathrm{m}^{-1}$ (commissioning) and $+2 \cdot 10^3\,\mathrm{m}^{-1}$ (MD6863), while Beam 2 has been dras-

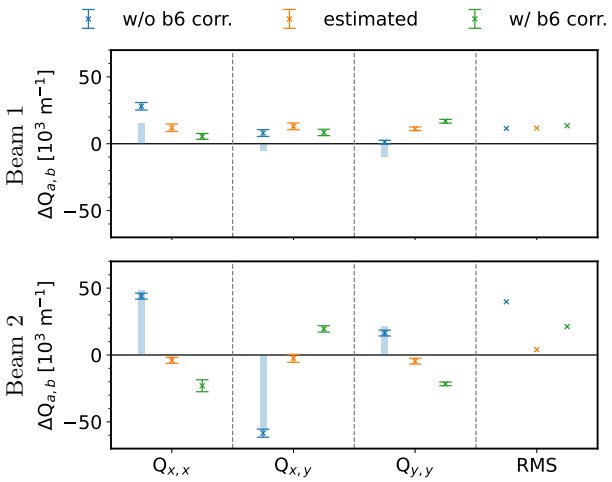

FIG. 5. Detuning shifts during MD6863, presented in the same manner as the data in Fig. 4.

tically improved by $-29 \cdot 10^3\,\mathrm{m}^{-1}$ (commissioning) and $-19 \cdot 10^3\,\mathrm{m}^{-1}$ (MD6863).

In general, despite the observed discrepancies between the expectation from simulation and measurement, both tested corrections are well able to reduce the common detuning introduced by high-order errors in the two beams, and partially even out the contribution per beam.

B. Error Sources

In addition, studies were carried out during MD to identify the sources of the errors, i.e. whether their origin lies in decapole or dodecapole order and if they stem from IR1 or IR5. To attain this objective, the crossing bump at IP1 was kept deactivated, while measurements were performed with nominal crossing angle in IP5 and also with opposite angle sign.

Multipole Order As there is only horizontal orbit in IP5 in our measurements (see Table I), we know from Eqs. (8) and (9) using the abbreviations Eqs. (11) and (12):

$$
\begin{aligned}
Q^{\emptyset}_{a,b} &= \sum_w K_4 L_w \tilde{\beta}_{a,b;w} \\
Q^{-}_{a,b} &= \sum_w \left(K_4 L_w - \Delta x_w K_5 L_w + \frac{1}{2}\Delta x_w^2 K_6 L_w \right) \tilde{\beta}_{a,b;w} \\
Q^{+}_{a,b} &= \sum_w \left(K_4 L_w + \Delta x_w K_5 L_w + \frac{1}{2}\Delta x_w^2 K_6 L_w \right) \tilde{\beta}_{a,b;w} \ ,
\end{aligned}
\tag{29}
$$

distinguishing between the cases "$\emptyset$" for flat-orbit, "+" for positive nominal crossing angle at IP5 and "−" for negative angle. Here it is also assumed that each element w sees an equal-in-magnitude but opposite in sign horizontal orbit offset x_w when switching crossing angle

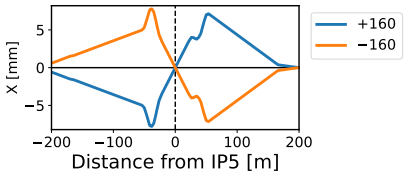

FIG. 6. Horizontal orbit of Beam 1 in IR5 for crossing schemes with ±160 µrad half-angles, demonstrating the symmetry with respect to the x-axis of the two scenarios.

sign as shown in Fig. 6. The contributions to the detuning change in IR5

$$
Q^{+}_{a,b} - Q^{\emptyset}_{a,b} = \sum_w \left(\Delta x_w K_5 L_w + \frac{1}{2}\Delta x_w^2 K_6 L_w \right) \tilde{\beta}_{a,b;w} \ ,
\tag{30}
$$

from each multipole order, can be calculated from the measured data using Eq. (29)

$$
\begin{aligned}
\sum_w \Delta x_w K_5 L_w \tilde{\beta}_{a,b;w} &= \frac{1}{2}\left(Q^{+}_{a,b} - Q^{-}_{a,b} \right) \\
\sum_w \frac{1}{2}\Delta x_w^2 K_6 L_w \tilde{\beta}_{a,b;w} &= \frac{1}{2}\left(Q^{+}_{a,b} + Q^{-}_{a,b} - 2Q^{\emptyset}_{a,b} \right) \ .
\end{aligned}
\tag{31}
$$

The results are presented in Fig. 7, which clearly shows that the main contribution to the detuning change in IR5 with positive crossing (blue) stems from dodecapole sources, while the contribution from decapoles is only around 14 % in RMS. This finding is in line with the expectation from magnetic measurements and simulations [25] as dodecapole fields are the first allowed harmonic of quadrupole magnets [35].

Another insight we achieve from Fig. 7, is that in Beam 1 the contributions from b_5 and b_6 add up, whereas in Beam 2 they partly cancel each other, leading to the higher detuning shifts measured in Beam 1 with positive IP5 crossing. We also see, that the b_6 corrections applied in IR5, calculated by Eqs. (8) and (9) and shown as green vertical bars, compensate the b_6 contribution in Beam 2 very well, but in Beam 1 only manage to do so for the horizontal term. This could be because no distinction was made between contributions from IR1 and IR5 when calculating the correction, which could be overcome by targeting also the IR5 measurement in Eq. (27); another reason could be, that β-function and orbit at the corrector magnets are not representative for β and orbit at the actual sources, making it impossible to find a perfect match.

In addition to these uncertainties about the error sources, also uncertainties about the correctors themselves can play a role: Assuming the corrector magnets to be misaligned with Gaussian distributions of $\sigma = 1\,\mathrm{mm}$ and a Gaussian distributed β-beating of $\sigma = 5\,\%$, the expected detuning can be calculated using the correction strengths "MD6863 w/ IP5" from Table III and Eq. (9).

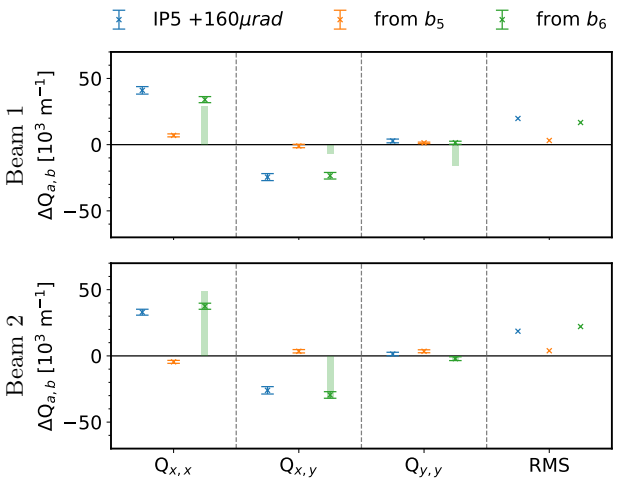

FIG. 7. Detuning changes between the scenario of positive crossing angle at IP5 and flat-orbit as measured during MD. Shown are the contributions to the full detuning change (blue) from decapole sources (orange) and dodecapole sources (green) as calculated from Eq. (31), for all detuning terms and the error-weighted root-mean-square (RMS) over all terms. Vertical bars show the detuning compensated by the correction "MD6863 w/o IP5" in Table III according to Eqs. (8) and (9). Measured values for the cross-terms $Q_{x,y}$ and $Q_{y,x}$ have been averaged.

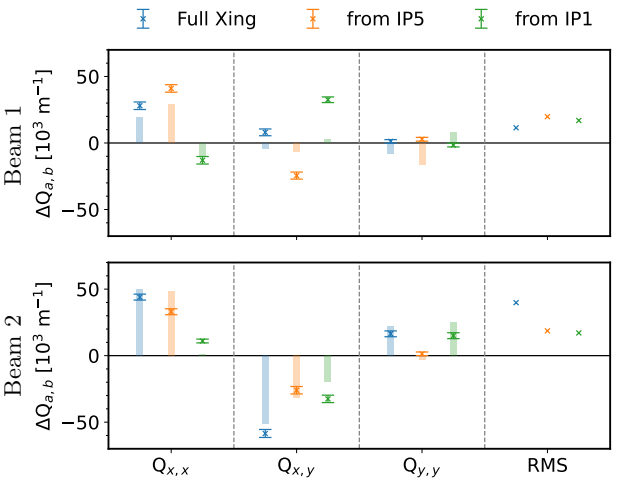

FIG. 9. Detuning changes as measured during MD without dodecapole correction between the detuning with full crossing and flat orbit (blue) as well as the scenario of positive crossing at IP5 (orange), for all detuning terms and the error-weighted root-mean-square (RMS) over all terms. For convenience, the detuning change on activating the crossing scheme at IP1 (green) has been calculated from the difference of the two measurements. Vertical bars show the detuning compensated by the correction "MD6863 w/o IP5" in Table III according to Eqs. (8) and (9).

The resulting detuning distributions are shown in Fig. 8 and have a mean standard deviation, over terms and beams, of $14 \cdot 10^3\,\mathrm{m}^{-1}$. Further simulations with the same parameters realizing only β-beating show a mean σ, over terms and beams, of $4 \cdot 10^3\,\mathrm{m}^{-1}$ while simulations realizing only misalignments give a mean σ of $13 \cdot 10^3\,\mathrm{m}^{-1}$, showing that including the measured β into calculations will not majorly improve the correction, as the uncertainty on alignments is the dominating factor. These values are compatible with the difference we see between expected and measured values after correction, meaning that there is a possiblity that without better knowledge of the corrector (mis-)alignments we could be at the limit of the correction accuracy.

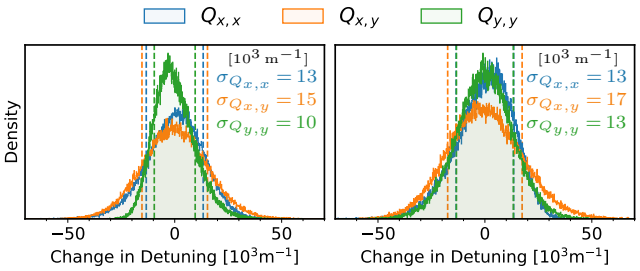

a) Beam 1 b) Beam 2

FIG. 8. Histograms of detuning changes for 100'000 realizations of random misalignments and random β-beating at the corrector elements. Both parameters are taken from Gaussian distributions: The distribution parameters for the misalignments are $\mu = 0\,\mathrm{mm}, \sigma = 1\,\mathrm{mm}$ and the for the β-ratio $\mu = 1, \sigma = 0.05$. The random values are applied individually to the corrector magnets left and right of IP1 and IP5. From each realization all three detuning terms were calculated from $Q_{a,b} = \sum_w \frac{1}{2}\left(\Delta x_w^2 - \Delta y_w^2\right)\tilde{\beta}_{a,b;w} K_6 L_w$ using the correction "MD6863 w/ IP5" in Table III for the strengths of the corrector elements w. The dashed vertical lines are set at the standard deviation of the resulting detuning distribution and their values are shown.

Interaction Region Figure 9 is showing again the shift in detuning between full-crossing scheme and flat-orbit as measured during MD before dodecapole corrections (blue), but this time split into contributions from the IR around IP5 (orange) and IP1 (green), where the former comes from the measurement with positive crossing angle at IP5 and the latter is calculated from the difference between the full crossing scheme and the IR5 measurements. The plots show that contributions from IR1 change sign between beams, whereas in IR5 the sign of the detuning shift stays the same. This leads to the IR contributions adding up in Beam 2 and cancelling each other partly in Beam 1, the opposite effect as discovered between b_5 and b_6 contributions in IR5. The effect from different orders is shadowed by the effect from different IRs, leading to the higher measured detuning shift with the full crossing scheme in Beam 2.

While the horizontal term shows a much larger contribution from IR5, the other terms are similar in absolute contribution from both IRs, leading to fairly equal RMS contributions from both IRs. This is in contrast to the

behaviour observed in 2018, where the main contribution had come from IR5; see Table II and [31]. The expected detuning to be compensated by the corrections, as calculated by Eqs. (8) and (9), are presented again through the vertical bars in Fig. 9: in total (blue) and split into the contributions per IR (orange and green). The correction seems to be good locally in only half of the terms, that is in the horizontal direct term of Beam 1 and in the cross-terms of Beam 2 as well as Beam 2's vertical direct term. Despite stronger powering of the IR5 correctors, over-correction of IR5 and under-correction of IR1 is only visible in Beam 2's $Q_{x,x}$ and $Q_{x,y}$, signifying that the difference in powering is an effect of the different orbit and β-functions at the correctors of the IRs and not of different error distributions between the IRs.

Improved Corrections Additional context about the locality and field order can be supplied to improve upon the corrections as discussed so far. This information, gained through the measurement of activating the crossing bump at the IPs individually, as well as with opposite sign, can be incorporated either through boundary restrictions on the linear equation system, as had been attempted in [69], or by including the measurements as additional targets into Eq. (27). The latter has been tested in simulations, and the results, presented in Fig. 10, are very promising: Despite the additional restrictions on the correction the estimated RMS does not change compared to the "global" correction. On the other hand, in all terms the correction is able to target b_6 in IP5 and the contribution per IP more closely than the previous correction, increasing locality of the correction.

These corrections have since been incorporated operationally into the LHC, replacing the commissioning corrections which were used from 04.06.2022 to 02.10.2022. Yet, due to the LHC running now for luminosity production, they could not be in detail investigated by amplitude detuning measurements.

C. Second-Order Detuning

Up until now, corrections were calculated based on the assumption that the second-order terms in amplitude in Eq. (7) are negligible and the main contribution to detuning from dodecapoles comes from feed-down to first-order detuning. Assuming the dodecapole fields from the correctors to be representative for the IR, just with opposite sign, the "MD6863 w/ IP5" correction calculated in the previous chapter and Eq. (10) could be used to calculate their contributions to second-order detuning. It was found that for large kicks, that is at 0.02 µm, the contributions could be up to 50 % of the total measured detuning.

To determine the influence of the second-order detuning on the first-order fits, two approaches have been tested: In the first approach, the measurement data has been fit with a second-order polynomial, still using ODR to include the measurement uncertainties. The second-order coefficients could in priciple then also be used to extent the equation system Eq. (27), adding new rows for the $\Delta Q^{(\mathrm{BN})}_{a,bc}$ on the left hand side, and new matrix elements from Eq. (10)

$$M^{(\mathrm{BN})}_{a,bc;w} = \tilde{\beta}^{(\mathrm{BN})}_{a,bc;w} \tag{32}$$

on the right hand side. As for example shown in Fig. 11, second-order polynomial fitting lead only to reasonable results where high kick-amplitudes could be reached (Fig. 11 top), yet lead to an overfitting on measurements where there maximum amplitude was below 0.01 µm and in conclusion to unreasonable and unusable results for most measurements (Fig. 11 bottom). This approach has hence been discarded for the data at hand, but could be usuable in future measurements if consitent large amplitude excitations can be achieved.

In the second approach, the values of the "MD6863 w/ IP5" corrections (Table III) at the correctors were used to calculate the tune shift from second order in amplitude at each conducted kick. These contributions have then been subtracted from the measured data, neglecting the errorbars on the corrections, but accounting for any coefficients due to the forced oscillations [42]. Subsequently, first-order polynomial fits were applied to the resulting data (e.g. shown in Fig. 11). The found detuning coefficients are given in Table IV, which also provides the differences to the original data in Table III. Despite the changes in detuning coefficients, the corrections evaluated from these and given in Table V, are still within 10 % of the originally calculated corrections, apart

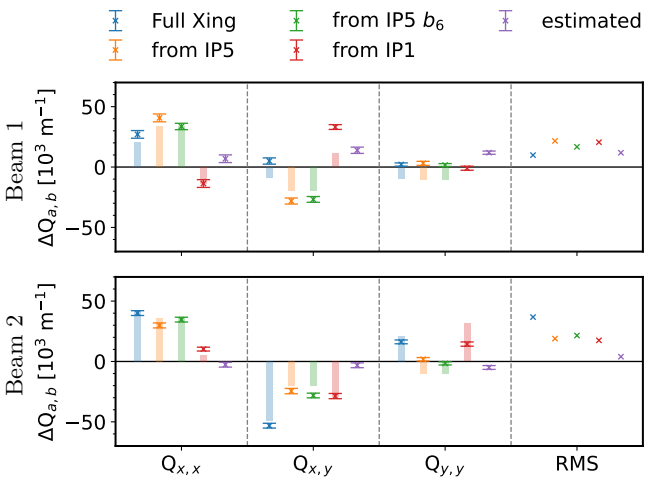

FIG. 10. Detuning changes as measured during MD without dodecapole correction between the detuning with full crossing and flat orbit in blue, as well as the measured individual contributions from the IR5 dodecapole fields in green, and the total contributions from IR5 (orange) and IR1 (red), as well as the estimated value after correction in purple. The data is presented for all detuning terms and the error-weighted root-mean-square (RMS) over all terms. Measured values for the cross-terms $Q_{x,y}$ and $Q_{y,x}$ have been averaged.

TABLE IV. Summary of amplitude detuning measurements after subtracting second-order contributions calculated from the "MD6863 w/ IP5" corrections (Table III) following the conventions in Table II. In parenthesis the difference (Δ) to the original detuning values are given.

	$Q_{x,x}$ $[10^3\,\mathrm{m}^{-1}]$ (Δ)	$Q_{y,x}$ $[10^3\,\mathrm{m}^{-1}]$ (Δ)	$Q_{x,y}$ $[10^3\,\mathrm{m}^{-1}]$ (Δ)	$Q_{y,y}$ $[10^3\,\mathrm{m}^{-1}]$ (Δ)
2022 MD6863 w/o b_6	-22 ± 2 (-4)	37 ± 2 ($+5$)	27 ± 4 ($+4$)	-7.7 ± 0.7 (-7.7)
flat-orbit	-27.1 ± 1.8 (-8)	19 ± 3 ($+6$)	23.9 ± 2.0 ($+12$)	-13.1 ± 0.8 (-16.5)
2022 MD6863 w/o b_6	6 ± 2 (-4)	42.2 ± 2.0 ($+5$)	30 ± 2 ($+3$)	-4.1 ± 1.0 (-6.1)
IP1&5 xing @ $\mp 160\,\mu$rad	17.5 ± 1.3 (-3.4)	-43 ± 3 (-4)	-31 ± 3 ($+12$)	4.8 ± 0.8 (-14.9)
2022 MD6863 w/o b_6	16 ± 2 (-7)	9 ± 3 ($+7$)	0.3 ± 1.4 ($+4.0$)	-6.2 ± 1.1 (-9.2)
IP5 xing @ $+160\,\mu$rad	5.8 ± 1.2 (-4.8)	-4 ± 3 ($+5$)	-6.5 ± 1.9 ($+9$)	-7.7 ± 0.6 (-13.0)
2022 MD6863 w/o b_6	3.0 ± 1.0 (-5.9)	8 ± 4 ($+5$)	3.2 ± 0.5 ($+4.1$)	-9.0 ± 0.4 (-9.2)
IP5 xing @ $-160\,\mu$rad	15.2 ± 1.8 (-5)	-11 ± 3 ($+4$)	-12.4 ± 1.4 ($+10.9$)	-16.4 ± 1.8 (-15)

TABLE V. Dodecapole-corrector strength values (K_6). In parenthesis the percentage of the maximum powering at 6.8 TeV is given. Shown are again the values for the *Improved Corrections* of "MD6863 w/ IP5" as in Table III as well as the corrector strenths calculated in the same manner from the detuning values of Table IV, with the second-order contributions subtracted.

	IP1		IP5	
	`MCTX.3L1` $[10^3\,\mathrm{m}^{-6}]$	`MCTX.3R1` $[10^3\,\mathrm{m}^{-6}]$	`MCTX.3L5` $[10^3\,\mathrm{m}^{-6}]$	`MCTX.3R5` $[10^3\,\mathrm{m}^{-6}]$
Original values	0.493 ± 0.192 (1%)	-3.982 ± 0.188 (11%)	5.003 ± 0.132 (14%)	-5.032 ± 0.162 (14%)
Second-order subtracted	0.816 ± 0.197 (2%)	-4.232 ± 0.202 (12%)	5.363 ± 0.142 (15%)	-5.011 ± 0.167 (14%)

from the corrector left of IP1 which almost doubled in strength, but is still lower than a quarter of the powering of the other correctors.

Interestingly, the correction strengths has overall been increased by this second approach, hinting at a compensation between first and second order terms. This approach could be extended to an iteration scheme, in the hopes that the corrector values will converge towards an optimal value. Due to time constraints and because the correction has not dramatically changed after this first iteration, this fine tuning has not been conducted. In fact, as most corrector values are within errorbars of each other (apart from the left corrector in IP5), it is doubtful that any difference would be perceptible given the accuracy of the measurements.

D. Comparison with the magnetic model

Magnets in the LHC have undergone magnetic measurements before installation, the results of which have been collected in the "Field Model of the LHC" (FiDeL [77]) which is the basis for the so called "Windows Interface to Simulation Errors" (WISE [78]). The errors on the field measurements lead to 100 different realizations, or "seeds", of the errors and are used to simulate realistic error scenarios in the LHC and HL-LHC.

In the past, differences had been found between corrections obtained from simulation and beam-based methods [79]. To test the agreement for the dodecapole corrections, a basic simulation has been set up, following the description in Section II G, but including dodecapole errors from the WISE tables. Previous studies have shown that, as the β-function for squeezed optics varies dramatically in the IR, the MQXA magnets of the triplets [6] should be split into hard-edge bodies and heads [21, 80, 81]. This procedure is applied to the simulation at hand. Errors are then locally corrected in IR1 and IR5 by minimizing dodecapole Resonance Driving Terms (RDT) in the IRs using the correction algorithm [82] presented in [83]. This means the correction target is inherently different to the beam-based measurements.

Figure 12 shows the simulated corrections in blue, compared to the three different beam-based corrections as in Table III from commissioning (orange), from MD without the IR5 measurements (green) and from the *Improved Corrections* including IR5 measurements ("MD6863 w/ IP5" in Table III, red). For completeness also the in Section III C explored correction values after subtracting the second-order contributions is shown (purple). While the beam-based corrections in IR1 fall right into the results from different seeds, they appear to be slightly stronger in the right corrector of IR5, yet still very close to the strength evaluated from some of the seeds. Hence, we find beam-based and magnetic measurements to agree very well within their uncertainties.

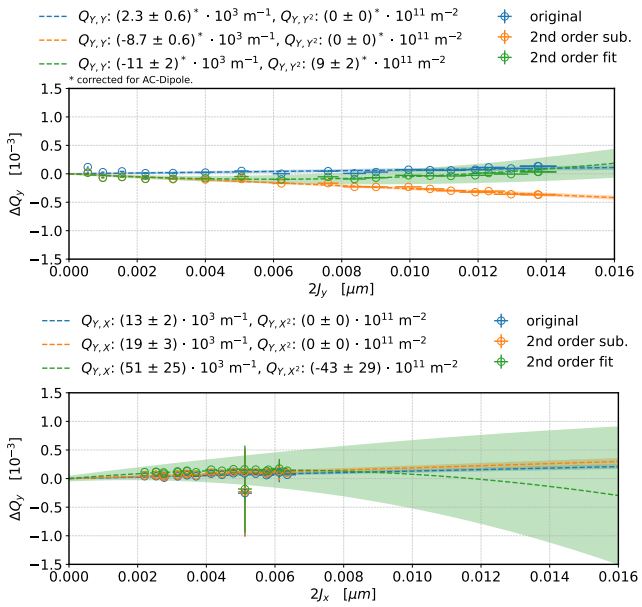

FIG. 11. Data of the measured vertical detuning in Beam 2 without dodecapole correction at flat-orbit from MD. Shown are linear polynomial fits on original measured data (blue) and the measured data after subtraction of the second-order contribution as calculated from the "MD6863 w/ IP5" corrections in Table III (orange). In green, the original data is shown again, but here a second-order polynomial fit is performed. Dashed lines show the polynomial fit to the data points, while the colored area covers one standard deviation of the fit. The constant part of the fit has been subtracted from the fit and its respective data points.

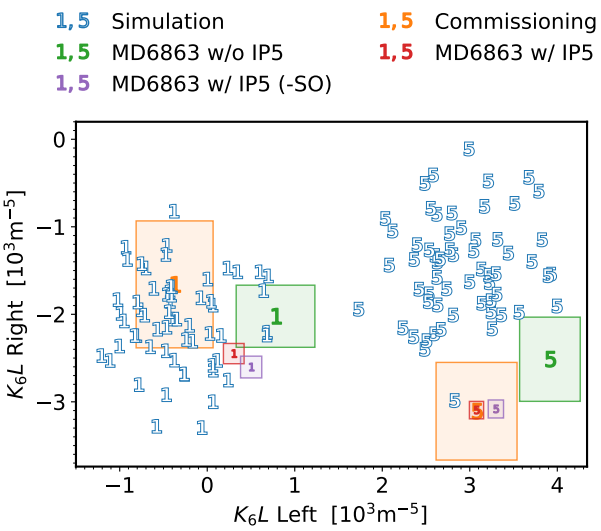

FIG. 12. Comparison of dodecapole corrections from simulations based on the magnetic model (blue), with the corrections calculated from the beam-based measurements of feed-down to amplitude detuning. The markers express the IR of the correctors: "1" for IR1 and "5" for IR5. In the simulation b_6 errors are assigned from 100 different WISE-seeds and corrected by minimizing dodecapole RDTs locally in the IRs. The plot shows the integrated strength of the right dodecapole corrector over the integrated strength of the left dodecapole corrector. The values of the beam-based corrections are as given in Tables III and V, where "(-SO)" refers to the values with second-order detuning subtracted, with their uncertainties represented by their surrounding area in the same colors.

E. Beam Lifetime

During the trims of the dodecapole corrections into the machine, beam lifetime has been extracted from the Beam Loss Monitors (BLMs) and beam intensity from the Fast Beam Current Transformer (BCTFR) and are shown in Fig. 13.

There is no obvious change on these parameters detectable after powering the dodecapole corrections, neither during commissioning (top plot) nor during MD (middle plot), when only non-colliding pilot bunches were circulating in the LHC. During operation, i.e. with colliding beams and a full filling scheme, trimming out the commissioning corrections and trimming in the *Improved Corrections* including IR5 measurements, the lifetime drops slightly during the trims and recovers thereafter, as seen in the bottom plot of Fig. 13. The histograms in Fig. 14 show that the mean beam-lifetime in the 41 s before trimming out the old corrections, between the two corrections and after trimming in the new corrections is preserved. This behaviour is expected in the LHC, where any change in parameters can lead to a temporary change in expected beam lifetime. There is no additional loss of beam intensity, apart from the visible burn-off due to collisions.

These measurements are in line with the measurements performed during MD3312 [40] and the studies performed in [25], in which the dodecapole correctors were powered to higher values before an impact on beam lifetime became visible.

IV. CONCLUSION AND OUTLOOK

In this paper, the results of the amplitude detuning measurements conducted during the LHC commissioning for Run 3 in 2022 and during a dedicated machine development session, have been presented, which were performed to identify and correct detuning originating in the feed-down from high-order nonlinear errors in the IRs. Dodecapole corrections were calculated, and for the first time integrated into the LHC operation, effectively reducing the RMS tune shift over all terms and both beams, therefore allowing e.g. for tighter control of Landau damping. Corrections calculated via this beam-based method agree very well with corrections calculated from local RDT minimization in simulations using the magnetic model. Incorporation of the corrections did not spoil beam-lifetime.

We have shown that with the measurement method at hand sources of the detuning could be identified: In

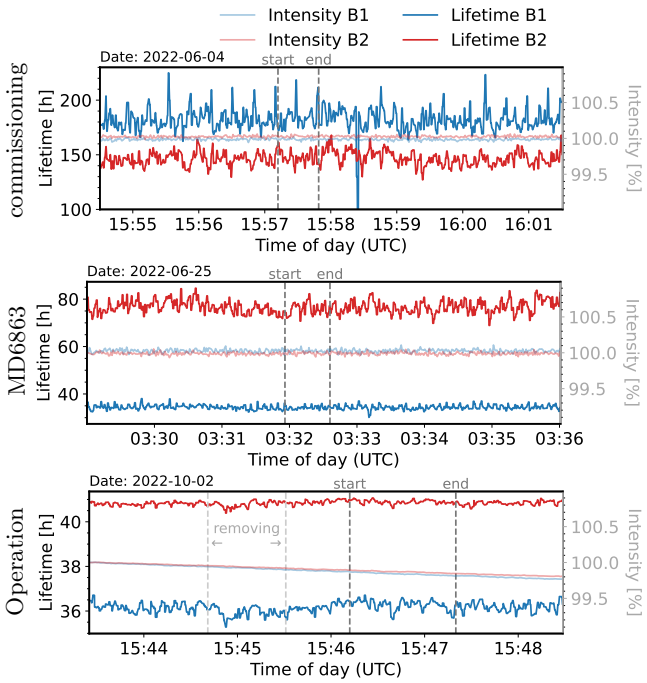

FIG. 13. Beam lifetime (from BLMs) and intensity (from BCTFR, normalized to the first datapoint) before and after the trim of the b_6 corrections during commissioning 2022 (top), MD (middle). The bottom plot shows the application of the "MD6863 w/ IP5" corrections (Table III), during operation, after trimming out ("removing") the previously incorporated dodecapole correction from commissioning. Start and end of the trimming processes are marked in the plot.

IR5 a clear origin from dodecapole errors has been seen and it could also be concluded that both IRs contribute equally to the observed detuning. To advance the corrections in the future, one could even further improve on the locality of the correction by targeting dodecapole contributions in both IRs specifically. To accomplish this, one more measurement with opposite-sign crossing angles is needed, either with crossing bumps around IP1 only, or opposite-sign full-crossing in both IRs.

As the presented results show, magnetic field errors up to dodecapole order can be identified using feed-down to amplitude detuning as observable. This can be achieved with our current measurement methods. For HL-LHC these results are vital, as the influence of high-order nonlinearities is foreseen to be increased. Not only confirms our study the expectations of [25], but also establishes that the therein described effort for high-order field error measurements can be reduced: Calculating the the dodecapole contribution from only three data points, instead of the suggested five, yields usable results, be it at the cost of statistics, which on the other hand are well accounted for at each of the data points themselves. Distinction between the different orders will become of more importance with the HL-LHC upgrade, as they can be targeted individually by the improved nonlinear corrector package, containing correctors for all normal and skew fields up to dodecapole order.

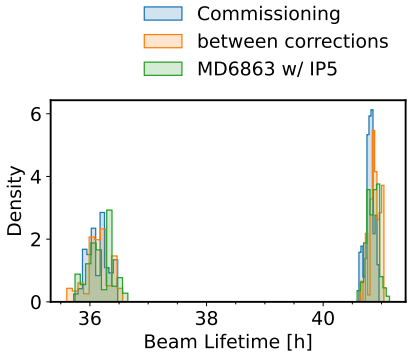

FIG. 14. Beam lifetime as histograms of the BLM data of 41 s intervals before trimming out the commissioning correction (blue), between corrections (orange) and after trimming in the improved correction, including all measurements from MD. The left cluster shows data from Beam 1 while the right cluster shows Beam 2 data. The same data over time can be seen in the bottom plot of Fig. 13.

Of further interest is also the study of the change in free and forced dynamic aperture upon applying the dodecapole corrections [57, 84].

V. ACKNOWLEDGEMENTS

The authors' copious thanks go to the CERN Operations Group and LHC Operators and Engineers in Charge, for the significant amount of support lent during commissioning and machine development sessions. Especially T. Argyropoulos, M. Hostettler and G. Trad who were managing the LHC during the measurements presented. Similarly, deep thanks go to the LHC Collimation team and CERN Beam Instrumentation Group, without their work amplitude detuning studies in the LHC would not have been possible. The authors want to also show their deep gratitude to B. Dalena for the discussion of the simulation results and for sharing data from their own studies about the ITs, P. Haagen for making the WISE error-tables available to us, as well as M. Giovannozzi for his help navigating different LHC error-tables. As always, great thanks go the LHC Optics Measurement and Correction team for their broad assistance during commissioning and in general all support given throughout the years. A heartfelt thank you also goes out to M. Hofer, for keeping his door open to any questions and for his help with the bibliography. J. Dilly would also like to thank Prof. Dr. A. Jankowiak for his wonderful PhD co-supervision and insightful comments.

[1] E. H. Maclean, in *Modelling and Correction of the Non-Linear Transverse Dynamics of the LHC from Beam-Based Measurements* (Herford College, University of Oxford, 2014).

[2] E. H. Maclean, R. Tomás, F. S. Carlier, M. S. Camillocci, J. W. Dilly, J. Coello de Portugal, E. Fol, K. Fuchsberger, A. Garcia-Tabares Valdivieso, M. Giovannozzi, M. Hofer, L. Malina, T. H. B. Persson, P. K. Skowronski, and A. Wegscheider, Phys. Rev. Accel. Beams **22**, 061004 (2019).

[3] X. Buffat, S. Antipov, G. Arduini, R. D. Maria, N. Karastathis, S. Kostoglou, A. Koval, E. Maclean, E. Métral, N. Mounet, Y. Papaphilippou, T. Persson, and R. Tomás, *Strategy for Landau Damping of Head-Tail Instabilities at Top Energy in the HL-LHC*, Accelerators & Technology Sector Note CERN-ACC-NOTE-2020-0059 (CERN, Geneva, Switzerland, 2020).

[4] A. Bazzani, G. Servizi, E. Todesco, and G. Turchetti, in *A Normal Form Approach to the Theory of Nonlinear Betatronic Motion*, CERN Yellow Reports: Monographs (CERN, Geneva, 1994).

[5] J. Gareyte, J. P. Koutchouk, and F. Ruggiero, *Landau Damping, Dynamic Aperture and Octupoles in LHC*, LHC Project Report 91 (CERN, 1997).

[6] O. S. Brüning, J. Poole, P. Collier, P. Lebrun, R. Ostojic, S. Myers, and P. Proudlock, LHC Design Report (2004).

[7] E. H. Maclean, R. Tomás, M. Giovannozzi, and T. H. B. Persson, Phys.Rev. ST Accel.Beams **18**, 121002 (2015).

[8] E. H. Maclean, F. Carlier, J. M. Coello de Portugal, A. Garcia-Tabares, M. Giovannozzi, L. Malina, T. Persson, P. Skowroński, and R. Tomás, in *IPAC2017* (Copenhagen, Denmark, 2017).

[9] J. Wei, W. Fischer, V. Ptitsin, R. Ostojic, and J. Strait, in *Proc. 1999 Part. Accel. Conf.* (IEEE, New York, NY, USA, 1999).

[10] O. S. Brüning, S. D. Fartoukh, A. M. Lombardi, F. Schmidt, T. Risselada, and A. Giovannozzi, in *1st LHC Proj. Workshop* (Chamonix, France, 2004).

[11] R. Tomás, M. Giovannozzi, and R. de Maria, Phys. Rev. ST Accel. Beams **12**, 011002 (2009).

[12] L. C. Teng, *Error Analysis for the Low Beta Quadrupoles of the Tevatron Collider / Location and Strengths of Correction Dipoles in the Low Beta Insertion*, Tech. Rep. FERMILAB-TM-1097 (Fermilab, 1982).

[13] Brdokhalren, Y. Luo, M. Bai, J. Beebe-Wang, J. Bengtsson, R. Calaga, W. Fischer, A. Jain, N. Malitsky, S. Peggs, F. Pilat, V. Ptitsyn, G. Robert-Demolaize, T. Satogata, S. Tepikian, D. Trbojevic, R. Tomas, Y. Luo, M. Bai, J. Beebe-Wang, R. Bengtsson, W. Calaga, A. Fischer, and Jain, *Overview of Magnetic Nonlinear Beam Dynamics in RHIC*, Tech. Rep. (2009).

[14] H. Sugimoto, *SuperKEKB*, Advanced Optics Control (CERN, 2015).

[15] M. Benedikt, J. Wenninger, D. Schulte, and F. Zimmermann, *Challenges for Highest Energy Circular Colliders*, Accelerators & Technology Sector Note CERN-ACC-2014-0153 (2014).

[16] D. Schulte, *Optics Challenges for Future Hadron Colliders*, Advanced Optics Control (CERN, 2015).

[17] E. Cruz Alaniz, R. Martin, E. H. Maclean, R. Tomas Garcia, and A. Seryi, in *Proc. 8th Int. Part. Accel. Conf. IPAC17* (JACoW, Copenhagen, Denmark, 2017) p. TUPVA038.

[18] O. Aberle, I. Béjar Alonso, O. Brüning, P. Fessia, L. Rossi, L. Tavian, M. Zerlauth, C. Adorisio, A. Adraktas, M. Ady, J. Albertone, L. Alberty, M. Alcaide Leon, A. Alekou, D. Alesini, B. A. Ferreira, P. A. Lopez, G. Ambrosio, P. Andreu Munoz, M. Anerella, D. Angal-Kalinin, F. Antoniou, G. Apollinari, A. Apollonio, R. Appleby, G. Arduini, B. A. Alonso, K. Artoos, S. Atieh, B. Auchmann, V. Badin, T. Baer, D. Baffari, V. Baglin, M. Bajko, A. Ball, A. Ballarino, S. Bally, T. Bampton, D. Banfi, R. Barlow, M. Barnes, J. Barranco, L. Barthelemy, W. Bartmann, H. Bartosik, E. Barzi, M. Battistin, P. Baudrenghien, I. B. Alonso, S. Belomestnykh, A. Benoit, I. Ben-Zvi, A. Bertarelli, S. Bertolasi, C. Bertone, B. Bertran, P. Bestmann, N. Biancacci, A. Bignami, N. Bliss, C. Boccard, Y. Body, J. Borburgh, B. Bordini, F. Borralho, R. Bossert, L. Bottura, A. Boucherie, R. Bozzi, C. Bracco, E. Bravin, G. Bregliozzi, D. Brett, A. Broche, K. Brodzinski, F. Broggi, R. Bruce, M. Brugger, O. Brüning, X. Buffat, H. Burkhardt, J. Burnet, A. Burov, G. Burt, R. Cabezas, Y. Cai, R. Calaga, S. Calatroni, O. Capatina, T. Capelli, P. Cardon, E. Carlier, F. Carra, A. Carvalho, L. Carver, F. Caspers, G. Cattenoz, F. Cerutti, A. Chancé, M. C. Rodrigues, S. Chemli, D. Cheng, P. Chiggiato, G. Chlachidze, S. Claudet, J. Coello De Portugal, C. Collazos, J. Corso, S. Costa Machado, P. Costa Pinto, E. Coulinge, M. Crouch, P. Cruikshank, E. Cruz Alaniz, M. Czech, K. Dahlerup-Petersen, B. Dalena, G. Daniluk, S. Danzeca, H. Day, J. De Carvalho Saraiva, D. De Luca, R. De Maria, G. De Rijk, S. De Silva, B. Dehning, J. Delayen, Q. Deliege, B. Delille, F. Delsaux, R. Denz, A. Devred, A. Dexter, B. Di Girolamo, D. Dietderich, J. Dilly, A. Doherty, N. Dos Santos, A. Drago, D.Drskovic, D. D. Ramos, L. Ducimetière, I. Efthymiopoulos, K. Einsweiler, L. Esposito, J. Esteban Muller, S. Evrard, P. Fabbricatore, S. Farinon, S. Fartoukh, A. Faus-Golfe, G. Favre, H. Felice, B. Feral, G. Ferlin, P. Ferracin, A. Ferrari, L. Ferreira, P. Fessia, L. Ficcadenti, S. Fiotakis, L. Fiscarelli, M. Fitterer, J. Fleiter, G. Foffano, E. Fol, R. Folch, K. Foraz, A. Foussat, M. Frankl, O. Frasciello, M. Fraser, P. F. Menendez, J.-F. Fuchs, S. Furuseth, A. Gaddi, M. Gallilee, A. Gallo, R. G. Alia, H. G. Gavela, J. G. Matos, H. Garcia Morales, A. G.-T. Valdivieso, C. Garino, C. Garion, J. Gascon, C. Gasnier, L. Gentini, C. Gentsos, A. Ghosh, L. Giacomel, K. G. Hernandez, S. Gibson, C. Ginburg, F. Giordano, M. Giovannozzi, B. Goddard, P. Gomes, M. Gonzalez De La Aleja Cabana, P. Goudket, E. Gousiou, P. Gradassi, A. G. Costa, L. Grand-Clément, S. Grillot, J. Guillaume, M. Guinchard, P. Hagen, T. Hakulinen, B. Hall, J. Hansen, N. Heredia Garcia, W. Herr, A. Herty, C. Hill, M. Hofer, W. Höfle, B. Holzer, S. Hopkins, J. Hrivnak, G. Iadarola, A. Infantino, S. I. Bermudez, S. Jakobsen, M. Jebramcik, B. Jenninger, E. Jensen, M. Jones, R. Jones, T. Jones, J. Jowett, M. Juchno, C. Julie, T. Junginger, V. Kain, D. Kaltchev, N. Karastathis, P. Kardasopoulos, M. Karppinen, J. Keintzel, R. Kersevan, F. Killing, G. Kirby, M. Korostelev, N. Kos, S. Kostoglou, I. Kozsar, A. Krasnov, S. Krave, L. Krzempek,

N. Kuder, A. Kurtulus, R. Kwee-Hinzmann, F. Lackner, M. Lamont, A. Lamure, L. L. m, M. Lazzaroni, M. Le Garrec, A. Lechner, T. Lefevre, R. Leuxe, K. Li, Z. Li, R. Lindner, B. Lindstrom, C. Lingwood, C. Löffler, C. Lopez, L. Lopez-Hernandez, R. Losito, F. Maciariello, P. Macintosh, E. Maclean, A. Macpherson, P. Maesen, C. Magnier, H. M. Durand, L. Malina, M. Manfredi, F. Marcellini, M. Marchevsky, S. Maridor, G. Marinaro, K. Marinov, T. Markiewicz, A. Marsili, P. Martinez Urioz, M. Martino, A. Masi, T. Mastoridis, P. Mattelaer, A. May, J. Mazet, S. Mcilwraith, E. McIntosh, L. Medina Medrano, A. Mejica Rodriguez, M. Mendes, P. Menendez, M. Mensi, A. Mereghetti, D. Mergelkuhl, T. Mertens, L. Mether, E. Métral, M. Migliorati, A. Milanese, P. Minginette, D. Missiaen, T. Mitsuhashi, M. Modena, N. Mokhov, J. Molson, E. Monneret, E. Montesinos, R. Moron-Ballester, M. Morrone, A. Mostacci, N. Mounet, P. Moyret, P. Muffat, B. Muratori, Y. Muttoni, T. Nakamoto, M. Navarro-Tapia, H. Neupert, L. Nevay, T. Nicol, E. Nilsson, P. Ninin, A. Nobrega, C. Noels, E. Nolan, Y. Nosochkov, F. Nuiry, L. Oberli, T. Ogitsu, K. Ohmi, O. R., J. Oliveira, P. Orlandi, P. Ortega, J. Osborne, T. Otto, L. Palumbo, S. Papadopoulou, Y. Papaphilippou, K. Paraschou, C. Parente, S. Paret, H. Park, V. Parma, C. Pasquino, A. Patapenka, L. Patnaik, S. Pattalwar, J. Payet, G. Pechaud, D. Pellegrini, P. Pepinster, J. Perez, J. P. Espinos, A. P. Marcone, A. Perin, P. Perini, T. Persson, T. Peterson, T. Pieloni, G. Pigny, J. Pinheiro de Sousa, O. Pirotte, F. Plassard, M. Pojer, L. Pontercorvo, A. Poyet, D. Prelipcean, H. Prin, R. Principe, T. Pugnat, J. Qiang, E. Quaranta, H. Rafique, I. Rakhno, D. R. Duarte, A. Ratti, E. Ravaioli, M. Raymond, S. Redaelli, T. Renaglia, D. Ricci, G. Riddone, J. Rifflet, E. Rigutto, T. Rijoff, R. Rinaldesi, O. Riu Martinez, L. Rivkin, F. Rodriguez Mateos, S. Roesler, I. Romera Ramirez, A. Rossi, L. Rossi, V. Rude, G. Rumolo, J. Rutkovksi, M. Sabate Gilarte, G. Sabbi, T. Sahner, R. Salemme, B. Salvant, F. S. Galan, A. Santamaria Garcia, I. Santillana, C. Santini, O. Santos, P. S. Diaz, K. Sasaki, F. Savary, A. Sbrizzi, M. Schaumann, C. Scheuerlein, J. Schmalzle, H. Schmickler, R. Schmidt, D. Schoerling, M. Segreti, M. Serluca, J. Serrano, J. Sestak, E. Shaposhnikova, D. Shatilov, A. Siemko, M. Sisti, M. Sitko, J. Skarita, E. Skordis, K. Skoufaris, G. Skripka, D. Smekens, Z. Sobiech, M. Sosin, M. Sorbio, F. Soubelet, B. Spataro, G. Spiezia, G. Stancari, M. Staterao, J. Steckert, G. Steele, G. Sterbini, M. Struik, M. Sugano, A. Szeberenyi, M. Taborelli, C. Tambasco, R. T. Rego, L. Tavian, B. Teissandier, N. Templeton, M. Therasse, H. Thiesen, E. Thomas, A. Toader, E. Todesco, R. Tomás, F. Toral, R. Torres-Sanchez, G. Trad, N. Triantafyllou, I. Tropin, A. Tsinganis, J. Tuckamantel, J. Uythoven, A. Valishev, F. Van Der Veken, R. Van Weelderen, A. Vande Craen, B. Vazquez De Prada, F. Velotti, S. Verdu Andres, A. Verweij, N. V. Shetty, V. Vlachoudis, G. Volpini, U. Wagner, P. Wanderer, M. Wang, X. Wang, R. Wanzenberg, A. Wegscheider, S. Weisz, C. Welsch, M. Wendt, J. Wenninger, W. Weterings, S. White, K. Widuch, A. Will, G. Willering, D. Wollmann, A. Wolski, J. Wozniak, Q. Wu, B. Xiao, L. Xiao, Q. Xu, Y. Yakovlev, S. Yammine, Y. Yang, M. Yu, I. Zacharov, O. Zagorodnova, C. Zannini, C. Zanoni, M. Zerlauth, F. Zimmermann, A. Zlobin, M. Zobov, and I. Zurbano Fernandez, *High-Luminosity Large Hadron Collider (HL-LHC): Technical Design Report*, CERN Yellow Reports: Monographs CERN-2020-010 (CERN, Geneva, 2020).

[19] G. Arduini, R. Bruce, R. D. Maria, M. Giovannozzi, G. Iadarola, J. Jowett, E. Métral, Y. Papaphilippou, and R. T. Garcia, in *High-Luminosity Large Hadron Collider (HL-LHC): Technical Design Report*, Vol. 10 (2020) pp. 17–17.

[20] F. S. Carlier, E. H. Maclean, L. E. Medina Medrano, L. Malina, D. Gamba, P. K. Skowronski, E. Fol, A. Wegscheider, A. Garcia-Tabares Valdivieso, and M. Giovannozzi, *Optics Measurements and Correction Challenges for the HL-LHC*, Accelerators & Technology Sector Note CERN-ACC-2017-0088 (2017).

[21] X. Buffat, F. Carlier, J. Coello De Portugal, R. De Maria, J. Dilly, E. Fol, N. Fuster Martinez, D. Gamba, Garcia-Tabares Valdivieso, Ana, H. Garcia-Morales, M. Giovannozzi, M. Hofer, N. Karastathis, J. Keintzel, E. H. Maclean, L. Malina, T. H. B. Persson, P. K. Skowronski, F. Soubelet, R. Tomás, F. Van Der Veken, L. van Riesen-Haupt, A. Wegscheider, D. W. Wolf, J. F. Cardona, B. Dalena, and T. Pugnat, *Optics Measurement and Correction Strategies for HL-LHC*, Accelerators & Technology Sector Note CERN-ACC-2022-0004 (CERN, 2022).

[22] E. H. Maclean, R. Tomás, F. Schmidt, and T. H. B. Persson, Phys. Rev. ST Accel. Beams **17**, 081002 (2014).

[23] E. H. Maclean, R. Tomás, F. S. Carlier, J. Coello de Portugal, E. Fol, K. Fuchsberger, A. Garcia-Tabares Valdivieso, M. Giovannozzi, M. Hofer, L. Malina, T. H. B. Persson, P. K. Skowronski, M. Solfaroli Camillocci, and A. Wegscheider, *Detailed Review of the LHC Optics Commissioning for the Nonlinear Era*, Accelerators & Technology Sector Note CERN-ACC-2019-0029 (2019).

[24] F. S. Carlier, *A Nonlinear Future: Measurements and Corrections of Nonlinear Beam Dynamics Using Forced Transverse Oscillations*, Ph.D. thesis (2020).

[25] E. H. Maclean, F. S. Carlier, J. Dilly, M. Le Garrec, M. Giovannozzi, and R. Tomás, Eur. Phys. J. Plus **137**, 1249 (2022).

[26] M. Gasior and R. Jones, *High Sensitivity Tune Measurement by Direct Diode Detection*, Tech. Rep. CERN-AB-2005-060 (2005).

[27] A. Boccardi, M. Gasior, O. Jones, and R. J. Steinhagen, *An Overview of the LHC Transverse Diagnostics Systems*, LHC Project Report LHC-PROJECT-REPORT-1166 (2009).

[28] A. Boccardi, M. Gasior, R. Jones, P. Karlsson, and R. J. Steinhagen, *First Results from the LHC BBQ Tune and Chromaticity Systems* (2009).

[29] E. H. Maclean, *LHC Optics Commissioning in 2018*, LMC Meeting (CERN, 2018).

[30] E. H. Maclean, *Nonlinear Optics MDs in 2018*, ABP-HSS Section Meeting (CERN, 2018).

[31] J. Dilly, M. Albert, T. Argyropoulos, F. Carlier, M. Hofer, L. Malina, M. S. Camillocci, and R. Tomas, *Report and Analysis from LHC MD 3311: Amplitude Detuning at End-of-Squeeze*, Accelerators & Technology Sector Note CERN-ACC-NOTE-2019-0042 (CERN, 2019).

[32] F. Pilat, Y. Luo, N. Malitsky, and V. Ptitsyn, in *Proc. 2005 Part. Accel. Conf.* (IEEE, Knoxville, TN, USA, 2005) pp. 601–605.

[33] E. H. Maclean, X. Buffat, F. Carlier, E. Fol, P. K. Skowronski, A. Garcia-Tabares Valdivieso, A. Wegscheider, T. H. B. Persson, R. Tomás, L. Malina, and J. Coello de Portugal, in *Evian* (2016) p. 9.

[34] E. H. Maclean, R. Tomás, F. Carlier, M. Solfaroli Camillocci, J. Coello De Portugal, E. Fol, K. Fuchsberger, A. Garcia-Tabares Valdivieso, M. Giovannozzi, M. Hofer, L. Malina, T. H. B. Persson, P. K. Skowronski, and A. Wegscheider (2017) p. 7.

[35] A. K. Jain, in *Proc. CERN Accel. Sch. Meas. Alignment Accel. Detect. Magn.* (CERN, Anacapri, Italy, 1997) pp. 1–26.

[36] J. Dilly, E. H. Maclean, and R. Tomás, in *Proc. 12th Int. Part. Accel. Conf. IPAC21* (JACoW, Campinas, Brazil, 2021) p. MOPAB259.

[37] J. Dilly, M. Giovannozzi, R. Tomás, and F. Van Der Veken, in *Proc. 13th Int. Part. Accel. Conf. IPAC22* (JACoW, Bangkok, Thailand, 2022) p. WEPOPT059.

[38] E. H. Maclean, A. Wegscheider, M. Hofer, L. Malina, B. Dalena, P. K. Skowronski, E. Fol, F. S. Carlier, A. Garcia-Tabares Valdivieso, M. Giovannozzi, J. Coello de Portugal, R. Tomás, J. Dilly, E. Cruz Alaniz, and M. Solfaroli Camillocci, *Report from LHC MD 2158: IR-nonlinear Studies*, Accelerators & Technology Sector Note CERN-ACC-2018-0021 (2018).

[39] E. H. Maclean, *Prospect for High-Order Optics Measurement in the High-Luminosity LHC*, ABP Information Meeting (CERN, 2020).

[40] J. Dilly, M. Albert, F. Carlier, M. Hofer, L. Malina, M. Solfaroli Camillocci, R. Tomas, J. Coello De Portugal, B. Dalena, E. Fol, E. H. Maclean, T. H. B. Persson, M. Spitznagel, and A. García-Tabarés Valdivieso, *Report from LHC MD 3312: Replicating HL-LHC DA*, Accelerators & Technology Sector Note CERN-ACC-NOTE-2022-0021 (CERN, Geneva, Switzerland, 2022).

[41] W. Fischer, J. Beebe-Wang, Y. Luo, and S. Nemesure, in *Proc. First Int. Part. Accel. Conf. IPAC10* (BNL-90739-2010-CP, Kyoto, Japan, 2010).

[42] S. White, E. H. Maclean, and R. Tomás, Phys. Rev. ST Accel. Beams **16**, 071002 (2013).

[43] H. Wiedemann, *Particle Accelerator Physics*, 4th ed., Graduate Texts in Physics (Springer International Publishing, Cham, 2015).

[44] J. Bengtsson and J. Irwin, *Analytical Calculations of Smear and Tune Shift*, Tech. Rep. (SSC Laboratory, 1990).

[45] E. H. Maclean, S. Redaelli, T. H. B. Persson, J. Uythoven, S. Moeckel, F. Schmidt, and R. Tomás, *Non-Linear Beam Dynamics Tests in the LHC: LHC Dynamic Aperture MD on Beam 2 (24th of June 2012)*, Accelerators & Technology Sector Note CERN-ATS-Note-2013-022 MD (CERN, 2013).

[46] T. Bach, M. Giovannozzi, A. Langner, Y. I. Levinsen, M. Ryoichi, E. H. Maclean, M. J. McAteer, S. Redaelli, P. K. Skowronski, R. Tomás, T. H. B. Persson, and S. White, *Measurement of Amplitude Detuning at Flat-Top and Beta*=0.6 m Using AC Dipoles*, Accelerators & Technology Sector Note CERN-ATS-Note-2013-015 MD (2013).

[47] R. Tomás, X. Buffat, S. White, J. Barranco, and E. H. Maclean, *Collecting Amplitude Detuning Measurements from 2012*, Tech. Rep. (2014).

[48] M. Bai, W. K. Van Asselt, F. Schmidt, M. Blaskiewicz, A. Lehrach, and T. Roser, in *Proc. 19th IEEE Part. Accel. Conf. PAC01* (JACoW, Chicago, IL, USA, 2001).

[49] R. Tomás, M. Bai, R. Calaga, W. Fischer, A. Franchi, and G. Rumolo, Phys. Rev. ST Accel. Beams **8**, 10.1103/PhysRevSTAB.8.024001 (2005).

[50] O. E. Berrig, R. Jones, J.-P. Koutchouk, W. Höfle, J. Koopman, F. Schmidt, and H. Schmickler, *Excitation of Large Transverse Beam Oscillations without Emittance Blow-up Using the AC-Dipole Principle*, Accelerators & Technology Sector Note CERN-SL-2001-019-BI (CERN, 2001).

[51] O. E. Berrig, W. Höfle, R. Jones, J. Koopman, J.-P. Koutchouk, and F. Schmidt, *Emittance-Conserving Transverse Excitation Using the "AC-Dipole" Principle.*, Accelerators & Technology Sector Note SL-Note-2000-062-MD (CERN, 2004).

[52] N. Catalan-Lasheras, S. D. Fartoukh, and J.-P. Koutchouk, *Linear Optics Measurements Using an AC-Dipole Excitation*, Tech. Rep. (2004).

[53] M. Bai, S. Y. Lee, J. W. Glenn, H. Huang, L. Ratner, T. Roser, M. J. Syphers, and W. van Asselt, Phys. Rev. E **56**, 6002 (1997).

[54] R. Tomás, Phys. Rev. ST Accel. Beams **8**, 024401 (2005).

[55] M. Wendt, ArXiv200514081 Phys. (2020), arXiv:2005.14081 [physics].

[56] S. Mönig, J. M. Coello de Portugal, T. Persson, A. Langner, R. Tomás, and E. Maclean, in *Proc. 7th Int. Part. Accel. Conf. IPAC16*, CERN-ACC-2016-173 (JACoW, Busan, Korea, 2016) p. THPMR044.

[57] F. S. Carlier, R. Tomás, E. H. Maclean, and T. H. B. Persson, Phys. Rev. Accel. Beams **22**, 13 (2019).

[58] OMC-Team, L. Malina, J. Dilly, M. Hofer, F. Soubelet, A. Wegscheider, J. M. C. De Portugal-Martinez Vazquez, M. L. Garrec, T. Persson, J. Keintzel, H. G. Morales, and R. Tomás, OMC3, CERN.

[59] L. Malina, *Novel Beam-Based Correction and Stabilisation Methods for Particle Accelerators*, Ph.D. thesis (2018).

[60] L. Malina, in *Proc. 13th Int. Part. Accel. Conf. IPAC22*, Vol. IPAC2022 (JACOW Publishing, Geneva, Switzerland, Bangkok, Thailand, 2022) p. WEPOMS035.

[61] J. Dilly, Amplitude Detuning - OMC Documentation (2022).

[62] A. Garcia-Tabares, F. Carlier, L. Malina, J. Coello de Portugal, A. Langner, P. Skowroński, E. Maclean, T. Persson, R. Tomás, and M. Solfaroli Camillocci, *Optics-Measurement-Based BPM Calibration*, Tech. Rep. (2016).

[63] A. García-Tabarés Valdivieso and R. Tomas, Phys. Rev. Accel. Beams **23**, 042801 (2020).

[64] R. Tomás, T. Bach, R. Calaga, A. Langner, Y. I. Levinsen, E. H. Maclean, T. H. B. Persson, P. K. Skowronski, M. Strzelczyk, G. Vanbavinckhove, and R. Miyamoto, Phys. Rev. ST Accel. Beams **15**, 10.1103/PhysRevSTAB.15.091001 (2012).

[65] T. Persson, F. Carlier, J. Coello de Portugal, A. G.-T. Valdivieso, A. Langner, E. H. Maclean, L. Malina, P. Skowronski, B. Salvant, R. Tomás, and A. C. G. Bonilla, Phys. Rev. Accel. Beams **20**, 10.1103/PhysRevAccelBeams.20.061002 (2017).

[66] A. Langner and R. Tomás, Phys. Rev. ST Accel. Beams **18**, 10.1103/PhysRevSTAB.18.031002 (2015).

[67] P. T. Boggs and J. E. Rogers, in *Contemporary Mathematics*, Vol. 112, edited by P. J. Brown and W. A. Fuller (American Mathematical Society, Providence, Rhode Is-

land, 1990) pp. 183–194.
[68] R. Gommers, P. Virtanen, E. Burovski, W. Weckesser, T. E. Oliphant, M. Haberland, D. Cournapeau, T. Reddy, Alexbrc, P. Peterson, A. Nelson, J. Wilson, Endolith, N. Mayorov, I. Polat, S. Van Der Walt, P. Roy, M. Brett, D. Laxalde, E. Larson, J. Millman, Lars, Peterbell10, A. Sakai, P. Van Mulbregt, C. Carey, Eric-Jones, R. Kern, Kai, and E. Moore, SciPy: Fundamental algorithms for scientific computing in python, Zenodo.
[69] J. Dilly, E. H. Maclean, and R. Tomás, in *Proc. 13th Int. Part. Accel. Conf. IPAC22* (JACoW, Bangkok, Thailand, 2022) p. WEPOPT060.
[70] T. Gläßle, Y. I. Levinsen, and K. Fuchsberger, Cpymad: Cython binding to MAD-X.
[71] CERN - Accelerator Beam Physics Group, Methodical Accelerator Design - MAD.
[72] E. Forest, F. Schmidt, and E. McIntosh, *Introduction to the Polymorphic Tracking Code*, SPS and LHC Division Note CERN–SL–2002–044 (AP) (2002).
[73] E. Forest, *From Tracking Code to Analysis* (Springer Japan, Tokyo, 2016).
[74] D. Jacquet, R. Gorbonosov, G. Kruk, and P. P. Mira, in *Proc. ICALEPCS2013*, Vol. THPPC058 (JACoW, San Francisco, CA, USA, 2014) p. 4.
[75] T. Persson, F. Carlier, J. Cardona, A. C. Ojeda, J. Dilly, H. G. Morales, V. Ferrentino, E. Fol, M. Hofer, E. J. Høydalsvik, J. Keintzel, M. L. Garrec, E. H. Maclean, L. Malina, F. Soubelet, R. Tomas, L. V. Riesen-Haupt, and A. Wegscheider, *Linear Optics Measurements and Corrections*, LHC Machine Committee (LMC #443) (CERN, 2022).
[76] E. H. Maclean, *Non-Linear Optics Measurements and Corrections*, LHC Machine Committee (LMC #443) (CERN, 2022).
[77] FiDeL - the magnetic model of the LHC.
[78] CERN - Accelerator Technology Department, Windows Interface to Simulation Errors.
[79] E. H. Maclean, *The B4 Issue Continues*, 3rd FiDeL Meeting Run III (CERN, 2020).
[80] T. Pugnat, S. Bagnis, B. Dalena, and C. Lorin, in *IPAC'21*, Vol. IPAC2021 (JACOW Publishing, Geneva, Switzerland, Campinas, Brazil, 2021).
[81] T. Pugnat, *3D non-linear beam dynamics for the LHC upgrades*, Ph.D. thesis, University Paris XI - Paris Sud (2021).
[82] OMC-Team and J. Dilly, IRNL RDT Correction, CERN.
[83] J. Dilly and R. Tomás, *A Flexible Nonlinear Resonance Driving Term Based Correction Algorithm with Feed-Down*, Accelerators & Technology Sector Note to be published (CERN, 2022).
[84] E. H. Maclean, M. Giovannozzi, and R. B. Appleby, Phys. Rev. Accel. Beams **22**, 034002 (2019).